The Importance of Back Contact Modification in $Cu_2ZnSnSe_4$ Solar Cells: the Role of a Thin MoO_2 Layer

S. Lopez-Marino[a,b*], M. Espíndola-Rodríguez[a], Y. Sánchez[a], X. Alcobé[c], F. Oliva[a], H. Xie[a], M. Neuschitzer[a], S. Giraldo[a], M. Placidi[a], R. Caballero[d], V. Izquierdo-Roca[a], A. Pérez-Rodríguez[a,e], and E.Saucedo[a]

[a] Catalonian Institute for Energy Research (IREC), Jardin de les Dones de Negre 1, 08930, Sant Adrià del Besòs, Spain

[b] Present address: Crystalsol GmbH, Simmeringer Hauptstraβe 24, 1110, Vienna, Austria

[c] Centres Científics i Tecnològics de la Universitat de Barcelona (CCiTUB). LLuís Solé i Sabarís 1-3, 08028, Barcelona, Spain

[d] Universidad Autónoma de Madrid, Applied Physics Department

Francisco Tomás y Valiente 7, 28049 Madrid, Spain

[e] Departament de Electrònica (IN2UB), Universitat de Barcelona, Martí i Franquès 1, 08028, Barcelona, Spain

*Corresponding author −e-mail address: simonlopez_iq@hotmail.com tel.: +43 67762096445

Abstract

$Cu_2ZnSn(S_xSe_{1-x})_4$ (CZTSSe) photovoltaic absorbers could be the earth-abundant and low toxicity replacement for the already commercialized $CuIn_{1-x}Ga_xSe_2$ (CIGS) thin film technology. In order to make this possible, specific research efforts applied to the bulk, front and back interfaces must be performed with the aim of improving CZTSSe performance. In this paper the importance of back contact modification to obtain high efficiency $Cu_2ZnSnSe_4$ (CZTSe) solar cells and to

increase a paramount and limiting parameter such as V_{OC} is highlighted. Several Mo configurations (monolayer, bi-layer and tri-layer) with different electrical and morphological properties are investigated in CZTSe solar cells. An optimum tri-layer configuration in order to minimize overselenization of the back contact during thermal annealing while keeping reasonable electrical features is defined. Additionally, a thin intermediate MoO_2 layer that results in a very effective barrier against selenization and innovative way to efficiently assist in the CZTSe absorber sintering is introduced. The use of this layer enhances grain growth and subsequently the efficiency of solar cells increases via major V_{OC} and FF improvement. An efficiency increase from 7.2% to 9.5% is obtained using a Mo tri-layer with a 20 nm intermediate MoO_2 layer.

Keywords: $Cu_2ZnSnSe_4$, MoO_2, $MoSe_2$, solar cells, back contact

1. Introduction

The earth abundant and low toxic semiconductor kesterite $Cu_2ZnSn(S_xSe_{1-x})_4$ (CZTSSe) has rapidly progressed in the last decade in terms of photovoltaic performance, reaching recently the value of 12.6% [1]. Despite this remarkable achievement, the foreseen value of 18-20% to allow for industrial production is still an ambitioned goal for the kesterite community [2-4]. When compared to the already commercialized and relatively close in terms of optical and electrical properties chalcogenide semiconductor $CuIn_{1-x}Ga_xSe_2$ (CIGS), relevant differences have been pointed out [5-7]. A narrower single phase existence region and higher thermal instability when synthesizing the material could be hindering the ambitioned kesterite progress [8-10]. Furthermore, a remarkable V_{OC} deficit when compared with the CIGS chalcopyrite cousin seems to be the issue most frequently reported as the major problem to overcome to definitively boost kesterite based devices efficiency [4, 11,

12]. The sources of this V_{OC} deficit have been mainly linked to potential fluctuations in the CZTSSe structure reducing the fundamental gap of the material and/or band gap fluctuations [12-14]. The presence of high concentration of defects in the bulk and at the interfaces of CZTSSe, compositional non-uniformities within the absorber and the inevitable co-existence of multiple secondary phases along with the kesterite absorber, are often mentioned in the literature as a plausible cause [4, 5, 14]. It seems clear that to improve CZTSSe devices changes in the processing conditions to maximize V_{OC} must be performed, with the bulk and interfaces of the material as paramount working areas. Whereas chemical etchings have proved to be an important tool to modify the properties of the p-n junction, and therefore improve V_{OC} among other parameters, changing the back contact interface led as well to significant improvements [15-21]. The present work is devoted to the modification of the properties of the Mo/CZTSe interface by using different Mo configurations (monolayer, bi-layer and tri-layer) and an innovative intermediate ultrathin MoO_2 layer in CZTSe solar cells.

Introducing changes to the conventional Mo back contact is necessary to minimize the decomposition reaction between CZTSSe and Mo reported in the literature [22]. This undesired reaction is tight to the presence of secondary phases, usually binaries of Cu, Zn and Sn, and also voids due to the volatility of some of the decomposition reaction products [19, 22]. It is important to note, that even the best devices reported in the literature exhibit holes at the back contact interface, causing a poor morphology that can affect the optoelectronic properties of the devices [1, 23]. Additionally, a thicker $MoSe_2$ layer can be formed by the uncontrolled reaction between the chalcogen, Mo and CZTSe known as overselenization, and thereby affecting as well the solar cells performance [21]. Nevertheless, despite it is commonly agreed that $MoSe_2$ can be

detrimental for solar cells when present in large amount, it seems also clear that is necessary to allow for a good ohmic contact at the back region [24-26]. So far, several layers have been introduced in addition to the Mo back contact with the aim of coping with its instability during the thermal annealing treatments. A TiN layer has proved to be an effective way to control the overselenization of the back contact, i.e. the $MoSe_2$ thickness. A thickness as low as 20 nm improved the V_{OC} more than 100 mV and the efficiency from 2.95% to 8.9% [21]. Moreover, an energy barrier at the back contact of 135 meV reported in the literature, was significantly reduced to a value of 15 meV by the introduction of a 100 nm TiN layer, reducing the series resistance, R_s, and increasing the efficiency [20]. A 10 nm i-ZnO layer between the Mo and the CZTSe absorber showed a morphology improvement of the back contact interface by reducing voids and minimizing the decomposition reaction, generating less secondary phases at this region identified with Raman spectroscopy. As a result, an important improvement in J_{SC} and FF increased the efficiency from 2% to 6% [19]. Similar results were reported for the pure sulfide, CZTS, using 30 nm of TiB_4 and 20 nm of Ag [27, 28].

Another interesting aspect related to the Mo back contact is its oxygen content; it has been reported for both CIGS and CZTSSe a beneficial effect for solar cell performance when present in a certain amount [29, 30]. In the case of CZTS, an increase in O content in the Mo back contact, via annealing in N_2 atmosphere at 550ºC for 10 min, coupled with an increase in Na content, led to a reduction of the MoS_2 layer after the thermal annealing, reducing considerably the R_S [30]. A similar effect, reducing $MoSe_2$ thickness, has been reported to be beneficial for CZTSSe solar cells, where 1% of O_2 was incorporated to the Mo during the sputtering process

[31].Thus, it can be inferred that the study of Mo oxidation processes and/or its oxides, MoO_2 and MoO_3 are highly relevant for the thin film solar cell community.

So far, the effect of a MoO_2 layer with varying thickness was only reported for CISe absorbers by Duchatelet et al., by oxidizing Mo coated SLG substrates in a tubular furnace for specific time. In this way, the formation of $MoSe_2$ was suppressed with minimum impact in the sheet resistance of the back contact [32]. Nevertheless, the use of this thermal growth method is limited in terms of layer homogeneity and thickness control. Furthermore, to obtain a controlled stoichiometry 1:2 in the Mo:O ratio can be also fairly complex. In consequence, we investigate for the first time the introduction of a controlled and thin MoO_2 layer thermally evaporated from the pure oxide powder in CZTSe solar cells. The layer results in an effective way to prevent the overselenization of the back contact even using as low thickness as 10 nm. As a result, we obtain a large improvement in solar cell performance, mainly related to a dramatic increase in V_{OC} and FF, but also shunt resistance, R_{SH}, linked with a remarkable change in CZTSe grain size. Furthermore, relevant structural changes in both $MoSe_2$ and CZTSe layers due to the presence of the MoO_2 layer will also be discussed.

2. Material and methods

$10x10$ cm^2 Mo coated soda-lime glasses were used as standard substrates. The substrates were cleaned with soap and submitted to sequential ultrasonic bath cleanings: acetone, isopropanol and deionized water. The time of the ultrasonic treatment for each solvent was 10 min at a temperature of 55 ºC. Finally, the substrates were dried with a nitrogen flux. Previous to the back contact deposition,

they were submitted to an additional surface treatment using radiofrequency (RF) plasma (100 W, 2×10^{-2} mbar Ar pressure, room temperature, 5 min).

Several Mo configurations (monolayer, bi-layer and tri-layer) were produced based on different DC magnetron sputtering (DC-sp) deposition conditions (Ac450 Alliance Concepts). To configure the back contact layouts up to 3 different conditions were used, and we named them after Mo_A, $Mo_{A'}$ and Mo_B. A layer of MoO_2 layer was introduced in some cases as part of the Mo back contact configurations, either on top of the monolayers and bi-layers and usually combined with a Mo_A cap layer with thickness ranging from 20 to 70 nm. The Mo sputtering conditions imposed can be seen in Table 1, and a comprehensive summary with all the info regarding layer type, thickness and sheet resistance of the final configurations is also listed in Table 2. The thickness of the layers was determined by X-ray fluorescence (XRF Fisherscope XVD) and the measurements were calibrated using reference samples which thickness was determined by SEM. A spot size of 1 mm and integration times of 45 s for each measurement point (usually a matrix of 16 points was taken to obtain the mean thickness value) were used. The accelerating voltage of the primary X-rays source was 50 kV and a Ni10 filter was used to reduce the background scatter radiation signal. The MoO_2 layer was thermally evaporated (Univex 250 from Oerlikon) from the pure oxide powder (99.99% Sigma Aldrich) at a deposition rate of 3 Å/s and a vacuum level of $\approx 4\times10^{-5}$ mbar using a tantalum boat. Additionally a 10 nm in thickness ZnO as intermediate layer was deposited prior to the absorber metallic stack by DC-sp (CT100 Alliance Concepts), using the same deposition parameters as for the i-ZnO window layer, which will be specified later on. The use of this layer is reported to minimize the decomposition reaction effects at the CZTSe/Mo interface during the absorber annealing. More details concerning its use can be found elsewhere

[19]. Before the CZTSe synthesis the substrates size is cut in smaller areas, usually around 2.5x2.5 cm^2 in all cases.

To synthesize the CZTSe absorbers, we employed a two stage process consisting in the deposition of metallic stacks followed by a reactive annealing process. The structure of the metallic stack precursor was the following: Cu(3nm)/Sn(262-275nm)/Cu(190-195nm)/Zn(170-178nm); all the metallic layers were deposited by DC-Sp (See reference [19] for detailed description of the deposition process). The thicknesses were selected in order to have the following final composition, further confirmed by XRF measurements: [Cu]/([Zn]+[Sn]) = 0.77 and [Zn]/[Sn] = 1.20-1.28. It has to be noted that in this case, the XRF values were calibrated using references samples analyzed by ICP.

The annealing process was carried out in a three zones tubular furnace, using a graphite box (69 cm^3 in volume). A two step thermal process consisting in a first treatment at 400 ºC during 30 min (heating ramp 20 ºC/min, dynamic Ar flow of 1.5 mbar) and a subsequent second treatment at 550 ºC during 15 min (heating ramp 20 ºC/min, total Ar pressure of 1 bar) was carried out. For the reactive atmosphere, 50 mg of Se (Alfa Aesar 99.999% purity) and 5 mg of Sn (Alfa Aesar 99.999% purity) were used. Se partial pressures during the annealing are estimated to be ~665 Pa (400 ºC) and ~14220 Pa (550 ºC). Finally, natural cooling down to room temperature was imposed.

Selected samples (Mo back contact configurations and/or CZTSe absorbers from full solar cells on SLG) were characterized by scanning electron microscope (SEM), Energy dispersed X-ray spectroscopy (EDX), time of flight secondary ion mass spectroscopy (TOF-SIMS), X-ray diffraction (XRD), Raman spectroscopy and four point probe resistivity methods. SEM images were taken using both a Zeiss Auriga

series and JEOL JSM-7100F field emission scanning electron microscopes, EDX elemental line scan analyses were made with 15 kV acceleration voltage using an INCA 250 series EDS detector from Oxford instruments on the cross section of selected selenized back contact configurations. XRD was performed using a PANalytical X'Pert PRO MPD Alpha1 powder diffractometer in Bragg-Brentano $\theta/2\theta$ geometry, from 4 to 145° with step size of 0.017° and integration time of 200 s per step, using Cu $K_{\alpha1}$ radiation ($\lambda = 1.5406$ Å). TOF-SIMS elemental depth profiles of complete CZTSe solar cells were obtained from a TOF-SIMS IV instrument from ION-TOF, using for sputtering a secondary O_2^+ ion gun operating at 2 keV, current of 421 nA and raster size of 350×350 μm^2. An area of 200×200 μm^2 was analyzed using a 25 KeV pulsed Bi_3^+ primary analysis Ion Gun. Raman microprobe measurements were performed with a LabRam HR800-UV Horiba-Jobin Yvon spectrometer coupled with an Olympus metallographic microscope. Backscattering measurements were made with 532.5 nm excitation wavelengths by focusing the laser spot onto the surface of the layers. In order to avoid effects in the spectra related to potential microscopic inhomogeneities, the spot was rastered over an area of 30x30 μm^2. The illumination power on the samples was kept below 0.4 mW to avoid presence of thermal effects in the spectra. Finally for the four point probe resistivity measurements a system from Everbeing Int'l Corp. was used

The as-annealed layers were submitted to an oxidizing chemical etching in acidic $KMnO_4$ solution (40 s) followed by a passivating $(NH_4)_2S$ (2 min) etching step (see ref. [16] and [18] for detailed description of the etching processes) to remove both ZnSe and Sn_xSe_y secondary phases. Additionally, a 2 min etching in a 2% KCN aqueous solution was also performed. Immediately after, and with the aim to complete the solar cells, a CdS layer was deposited by chemical bath deposition (60

nm in thickness) [33], i-ZnO (50 nm) and Sn_2O_3:In 350 nm, $50\Omega\square$) both by pulsed DC-Sp (CT100 Alliance Concepts). After TCO deposition all solar cells were submitted to an annealing in air at 200ºC for 30 minutes. 3x3 mm^2 cells were scribed using a micro-diamond scriber (MR200 OEG) and then J-V dark and illuminated curves (AM1.5 illumination conditions) could be obtained using a pre-calibrated Sun 3000 Class AAA solar simulator from Abet Technologies. The spectral response was measured in a pre-calibrated Bentham PVE300 system, allowing us to obtain the external quantum efficiency (EQE) of the cells.

The experiments performed in this work can be divided in two different parts. The first part is devoted to the comparison between Mo monolayers and bi-layers and the impact of the introduction of a thin MoO_2 layer (10 and 20 nm) along with a sacrificial Mo_A cap layer (30 nm) in these configurations with respect to back contact selenization and CZTSe solar cells optoelectronic properties.

The second part focuses on the impact of a Mo_A cap layer thickness (from 20 to 70 nm), as part of a tri-layer configuration, with and without an intermediate 20 nm MoO_2 layer on the optoelectronic parameters of CZTSe solar cells. A graphical summary with the back contact layouts for the different experimental parts is included in Figure 1.

3. Results and discussion

3.1. Experiment 1: Comparison between Mo Mono- and Bi-layer and Impact of the Thickness of Intermediate MoO_2 Layer in Back Contact Selenization and CZTSe Solar Cells

As previously stated, one of the major drawbacks that CZTSSe technology suffers from is the degradation of the Mo back contact usually coupled with the formation of

a thick MoS(e)$_2$ layer and the presence of many voids at this interface. Our previous works on CZTSe were based on Mo monolayers sputtered with high kinetic energy conditions (Mo$_A$), which can be checked in **Table 1** [19, 34]. The effects of the back contact degradation after selenization can be clearly observed in **Figure S1** of the Supporting information (S.I.).

In order to cope with this problem at the back interface, multilayer configurations were designed. Such complex layered structures have been frequently reported in the literature. Their use is linked with the widely accepted fact that properties such as good adhesion and low resistivity can be hard to obtain at the same time [35-37]. In our particular case when using low pressure conditions and high power density for the Mo deposition, our films showed good electrical features, sheet resistance ~ 0.2-0.3 Ω/sq for 800 nm of Mo$_A$, but no poor adhesion properties in contrast with the literature [35, 37]. Nevertheless, as it was shown in **Figure S1** of the S.I., a severe problem of overselenization usually took place. Therefore, we decided to invert the typical stack order of bi-layers configuration in terms of pressure that is commonly reported in the literature: bottom/high pressure and top/low pressure, in order to deal with this problem. The main reason to do so, is that an increase in the sputtering pressure can lead to a higher incorporation of O$_2$ from the background sputtering environment reducing the formation of MoSe$_2$ [31]. This can be due to a more porous structure with more intergranular space where impurities can be adsorbed and/or diffuse [36, 38].

In order to understand the impact of the sputtering conditions onto the Mo structure XRD measurements of Mo$_1$, Mo$_2$ and Mo$_3$ have been carried out. The Diffractograms are shown in Figure 2.

All the back contacts present the cubic structure typical for Mo (JCPDS-0-42-1120) with preferred orientation in the (110) planes. It is easy to notice that the bi-layers show wider and more asymmetric peaks than the monolayer, and this could be due to the fact that the upper part of the bi-layers (Mo_B) is obtained at an Ar pressure higher than the one used for the monolayer, leading to a slightly less compact layer with commonly lower macroscopic stress but with higher microstrains and smaller crystallites [36, 39, 40].

The differences in the morphology between Mo_A and Mo_B type layers can be checked via SEM images shown in **Figure S2** of the S.I.

Likewise, the impact on the electrical properties can be observed in **Table 2** by looking at the sheet resistance obtained by the four-point probe method. The monolayer has higher electrical conductivity than Mo_3 and Mo_2, in this order, being again directly linked to the sputtering deposition conditions. Furthermore, when the MoO_2 layer is introduced as part of the back contact designs no significant changes can be measured in the sheet resistance, at least up to 20 nm of MoO_2, this is due to its metallic electrical conductivity features [41].

To test the resilience against selenization of the different back contacts of Experiment 1, a selenization following the steps reported in the experimental section was carried out with all the back contact structures. **Table 3** shows the XRF estimated values for the $MoSe_2$ layer thickness formed after the annealing and the thickness for the non selenized underlaying Mo layer (Note that all the Mo configurations with MoO_2 intermediate layers have a 30 nm Mo_A sacrificial top layer). At a first glance it is obvious that Mo_1 is overselenized compared with Mo_2 and Mo_3, which barely have formed $MoSe_2$ (688 nm of $MoSe_2$ against 84/75 nm respectively). Additionally, SEM and EDX analyses were performed in a cross section configuration of samples Mo_1,

Mo_1-$10MoO_2$ and Mo_1-$20MoO_2$ in **Figure 3**. The effects of the introduction of 10 and 20 nm of MoO_2 as intermediate layer, deposited on top of Mo_1 with a sacrificial 30 nm cap layer of Mo_A (easily selenized as it has been shown) after the selenization process can be seen in that image. **Figures 3**a and d show a SEM cross sectional image of Mo_1 obtained with both secondary and back scattered electron detectors respectively. It seems clear that a large $MoSe_2$ layer arises after selenization, visualized between the red and the orange lines. When the MoO_2 layer is introduced the formation of $MoSe_2$ is clearly reduced already with a thickness of 10 nm (**Figure 3**b and 3e) if we compare the layer between the red and the orange lines with the reference case. Surprisingly, **Figure 3**c and f show slightly larger $MoSe_2$ formation when a 20 nm MoO_2 layer is introduced. This could be explained by possible local differences in the homogeneity of the evaporated layer, since the results from XRF (integrated over a much larger area than the SEM and EDX cross sectional analysis) point to similar or even lower formation of $MoSe_2$ and likewise for the remaining Mo after the thermal process (see **Table 3**). Further confirmation of the $MoSe_2$ reduction can be noticed by comparing the colored areas of the EDX elemental depth line scans of Figures g, h and i belonging to Mo_1, Mo_1-$10MoO_2$ and Mo_1-$20MoO_2$ respectively. The area marked corresponds to the thickness of the $MoSe_2$ layer.

By focusing again on **Table 3**, it is interesting to see how the bi-layers, Mo_2 and Mo_3, act as natural barriers against selenization (cases Mo_2 and Mo_3). Nevertheless, when introducing the MoO_2 layer, 10 and 20 nm, the selenization is further reduced since despite having a larger value of $MoSe_2$ thickness compared with the reference cases, we should take into account that a sacrificial 30 nm Mo_A cap layer was also introduced. Therefore, we should leave out the thickness of the $MoSe_2$ layer intentionally grown on top of the MoO_2 layer, which in a rough estimation could be

about 100 nm. In any case if we look at the value of the remaining Mo (non selenized) for the selenized bi-layers with 10 and 20 nm MoO_2, the value is larger than for the reference cases, Mo_2 and Mo_3, confirming the effectiveness of this oxide layer as Se barrier.

To understand the impact of the selenization on the structure of the different back contact configurations, XRD analysis of the selenized back contacts of Experiment 1 were performed (All the peaks have been indexed with the card JCPDS-3-65-3481). Nevertheless, before addressing this point a brief description of the $MoSe_2$ structural properties and their implications on solar cell performance are revised. $MoSe_2$ is a p-type semiconductor and layered compound with an indirect bandgap of 1.4 eV. It has a hexagonal structure based on sandwiched Se-Mo-Se sheets [24, 42-44]. It is important to note that this compound can be present in the solar cells with two main crystalline orientations, with the c-axis either parallel or perpendicular to the substrate [45, 46]. These two different orientations differ in adhesion and electrical properties, due to the different alignment of the $MoSe_2$ multilayered structure with respect to the substrate [42]. When the c-axis is perpendicular to the substrate, then the $MoSe_2$ sheets are parallel to the same, creating a natural barrier for selenization but weakening its bonding strength to the Mo and reducing its electrical conductivity. If the c-axis is parallel, then the $MoSe_2$ layers are oriented perpendicular to the Mo substrate increasing the adhesion and the electrical conductivity, but also the degree of Mo selenization [47, 48].

Figure S4 of the S.I. shows the difference between the monolayer Mo_1 and the bi-layers Mo_2 and Mo_3 when undergoing our standard selenization process. As it was confirmed by XRF an important reduction of the $MoSe_2$ formation can be noticed since the 100 and 110 diffraction peaks, typical for the $MoSe_2$ with the c-axis parallel

to the substrate, are dramatically reduced when comparing Mo_1 with Mo_2 and Mo_3. The role of 10 and 20 nm intermediate MoO_2 layer combined with a 30 nm Mo_A cap layer on the $MoSe_2$ structure and formation is presented in **Figure 4**a and b, for the case of a Mo_1 monolayer and a Mo_3 bi-layer respectively (note that the behavior of Mo_2 is similar to Mo_3). In the case of Mo_1 intense diffraction 100 and 110 peaks confirm the overselenization of this type of back contact. These peaks correspond to typical orientations for $MoSe_2$ with the Se-Mo-Se sheets oriented perpendicular to the substrate, i.e. c-axis parallel to the same. In contrast, when adding either 10 or 20 nm of MoO_2 the intensity of these peaks is strongly reduced, despite having 30 nm of a sacrificial Mo_A layer, which will be easily selenized. Interestingly, when looking at lower diffraction angles, a remarkable change in texture of the $MoSe_2$ formed can be observed when introducing the MoO_2 layer. This is due to the contribution of the (001) orientation, mainly driven by 002 but also 004 diffraction peaks. In this case, Se-Mo-Se sheets oriented parallel to the substrate, i.e. with c-axis being perpendicular to the same, seem to be growing due to the presence of the MoO_2 layer. Furthermore, a correlation with the thickness of the MoO_2 layer and the intensity of the $MoSe_2$ 002 diffraction peak can be drawn. Finally, an additional diffraction peak, 103, emerging from the background can be assigned to the mixture of the two main $MoSe_2$ crystalline orientations, as it has been reported in the literature [48]. Structural surface sensitive analyses were also performed in this set of samples using Raman spectroscopy. The results are shown in **Figure S4** of the S.I.; it can be clearly seen again a change in texture when comparing the samples with and without MoO_2 layer, due to the difference in the relative intensity between the most intense Raman modes. In the case of the bi-layers, the XRD analyses are very similar, so that only the case of Mo_3 is shown in **Figure 4**b. It can be easily noticeable, as already confirmed by XRF,

that the formation of $MoSe_2$ is reduced when using this type of complex Mo structure. The most intense and typical diffraction peaks for $MoSe_2$, 100 and 110, are relatively small (see black line of **Figure 4**b). When introducing the MoO_2 layer (red and blue lines) the intensity of those peaks is bigger, but this is due to the contribution of the $MoSe_2$ coming from the additional 30 nm Mo_A cap layer. Therefore, the MoO_2 layer for this case seems to be not necessary to avoid overselenization of the Mo back contact. Additionally, the 002 diffraction peak typical for $MoSe_2$ with c-axis perpendicular to the Mo surface remain unchanged in contrast with the monolayer case.

Up to now, it seems clear that MoO_2 is reducing the selenization of the Mo and induces changes in the orientation of the $MoSe_2$ when growing in contact with this layer, at least for the case of Mo_1. A reasonable question to make at this stage was whether this oxide is selenized, partially selenized or not? According to the thermodynamic analysis of Duchatelet et al., the selenization reaction for this oxide is thermodynamically much more demanding in energy than the reaction between Mo and Se, and thereby it can be inferred that the oxide cannot be selenized [32]. The free energy of Gibbs of the selenization reactions that could compete in the annealing processes is presented below:

$$Mo + Se_2 \rightarrow MoSe_2 \qquad \Delta rG^0 \ (900 \ K) = -129 \ KJ/mol \qquad (1)$$

$$MoO_2 + Se_2 \rightarrow MoSe_2 + O_2 \qquad \Delta rG^0 \ (900 \ K) = +294 \ KJ/mol \qquad (2)$$

The Gibbs free energy of reaction (1) is lower than the one of MoO_2 with Se, thus reaction (2) is not thermodynamically favored compared with the reaction of the Mo with Selenium. Therefore it can be concluded that is highly unlikely that the MoO_2 layer could be selenized.

In order to go further on the structural changes induced by this layer, selenization tests using similar configurations to the ones presented in **Figure 1** when using MoO_2, but with no additional Mo_A cap layer were performed. In this way, more light could be shed for instance on the specific location of the $MoSe_2$ layer with the c-axis growing perpendicular to the Mo surface, which usually is reported to be at the $MoSe_2$/absorber interface [48]. Specifically, 10, 20 and 30 nm of MoO_2 layers were grown on top of both monolayers and bi-layers to look at the $MoSe_2$ structural changes induced by this oxide. The results are shown in **Figure 5**.

By looking at **Figure 5**a (Mo_1 case), it is possible to draw a correlation with a thicker $MoSe_2$ layer with the c-axis perpendicular to the substrate and a thicker MoO_2 layer (navy blue). A strong texturing of the $MoSe_2$ in the (001) direction occurred (intense 002 difraction peak with regard to 100 peak), specially for the 10 nm MoO_2 layer, in agreement with the fact that for this experimental run this layer thickness results in a much more efficient barrier for selenization than thicker layers (20 and 30 nm). The results are similar than the ones shown in **Figure 4**a of the main document, but with poorer results in terms of Se barrier for the 20 nm MoO_2 layer. If the MoO_2 layer cannot be selenized due to un-favored thermodynamics, then the $MoSe_2$ that is formed should come from the underneath Mo layer. This might be due to uncompleted coverage or cracks on the relatively thin MoO_2 layers, being online with results reported by Duchatelet et al. for thin thermally oxidized grown MoO_2 layers [32]. In conclusion, if we look again to **Figure 3** of the main document, the $MoSe_2$ formed due to non homogeneities of the MoO_2 layer should be comprised between the green and the orange solid lines in Figures b and c, and between the dashed green and orange lines for Figure e and f. Moreover, it is possible to confirm the integrity of the MoO_2 layer after selenization since the most intense diffraction peaks for this

compound with monoclinic structure can be identified: (011), (020) and (220) (JCPDS-04-008-2624) (note that 020 and 220 are the most intense of several overlapped diffraction peaks). The fact of not being able to distinguish the oxide for the 20 and 10 nm layers might be related with the limitations of the XRD technique in θ-2θ configuration (Bragg-Brentano).

Focusing now on **Figure 5**b (Mo_3 case), again it is possible to correlate the $MoSe_2$ growth with the Mo-Se-Mo sheets parallel to the substrate with the thickness of the MoO_2 grown on top of Mo_3. This is in contrast with what it was observed in **Figure 4**b of the main document, but in that case a sacrificial Mo_A cap layer was grown on top of the MoO_2, and it might prevent or affect to some extension the formation of $MoSe_2$ with the c-axis perpendicular to the Mo surface.

It should be noted that so far the orientation of $MoSe_2$ grains has been linked with temperature processing, Se partial pressure, absorber composition, Mo orientation and Na content [24, 25, 42, 45, 46, 48, 49]. We report for the first time the induction of the growth of $MoSe_2$ grains with the c-axis perpendicular to the Mo substrate, i.e. acting as a natural Se barrier, when depositing a thin MoO_2 layer on the Mo back contact before selenization. The possibility of controlling the amount of $MoSe_2$ sheets growing parallel to the Mo substrate can be directly linked to the thickness of the MoO_2 layer, and thereby its beneficial properties could be maximized, avoiding its detrimental characteristics, i.e. poor electrical features and delamination issues.

Likewise, the contribution of the MoO_2 layer from the XRD pattern when its thickness is 30 nm for the Mo_3 bi-layer is even clearer than for the monolayer case. Moreover, Raman spectroscopy was also performed in this set of samples and the spectra are shown in **Figure S5**. Again, a clear texture change of the $MoSe_2$ layer growing in contact with the MoO_2 layer is confirmed (for more details see the S.I.)

All the back contact configurations presented in Experiment 1 were implemented as part of CZTSe solar cells. First, a comparison of cells performance based on plain monolayers (Mo_1) and bi-layers (Mo_2 and Mo_3) is shown in **Figure 6** via illuminated J-V curves along with a summary of the main optoelectronic parameters, and cross sectional SEM images of completed solar cells. At a first glance, by looking at **Figure 6**a it seems obvious that CZTSe cells based on monolayer back contact perform better than the Mo_2 and Mo_3 bi –layer based cells, 7.3% versus 4.7% and 5.7% respectively. An important degradation in V_{OC} and/or FF seemed to take place. Interestingly, when looking at **Figure 6**b and c, it can be seen that the cell performing better is the one that presents larger back contact interface degradation along with a thicker $MoSe_2$ layer (See **Figure S6** of supporting information for better comparison of both back contact interface morphologies). As already mentioned, those features are usually reported as undesired in order to allow for high efficient devices [21, 50]. Nevertheless, it has been also reported that a $MoSe_2$ layer could act as buffer layer between the Mo and the absorber, promoting an ohmic contact, and thereby improving the electrical transport. By looking at the absorber/Mo back contact interface of images b and c, it seems obvious that bi-layers might led to a too small $MoSe_2$ layer, insufficient to promote a good band alignment to avoid hole blocking transport and recombination of minority carriers at this interface [24-26]. The $MoSe_2$ layer can barely be seen by looking at the SEM images, which correlates also with the small values of $MoSe_2$ thickness obtained by XRF in **Table 3**. As a result, it can be concluded that an efficient tuning of the $MoSe_2$ thickness is of the utmost importance in order to boost CZTSe devices performance. In consequence, we can conclude that bi-layers are suitable structures to cope with overselenization but they need to be combined with a sacrificial Mo_A cap layer in order to produce a $MoSe_2$ layer with the

adequate thickness to avoid a high series resistance (R_S) and to promote a good band alignment of the back contact interface. This is the reason that led us to investigate the influence of the Mo_A cap layer as part of a tri-layer Mo configuration in Experiment 2. As an example, **Figure S7** of the S.I. shows a cross sectional SEM image of a tri-layer (Mo_4 back contact type) with 30 nm Mo_A cap layer. A ~100 nm $MoSe_2$ in thickness has grown between the absorber and the Mo. It should be noted that recently another way to control overselenization and $MoSe_2$ thickness growth at the back contact of CZTSe solar cells has been reported by Li et al [50].

Nevertheless, this work relies in a prealloying step at low temperature to control the $MoSe_2$ thickness, and thereby it would be only interesting when synthesizing CZTSe from metallic precursors. In the present work, the Mo tri-layer that we have defined offers an easy and flexible way adaptable for all CZTSe precursors, since even when selenizing bare Mo-tri-layers the $MoSe_2$ that is formed is clearly determined by the Mo_A cap layer thickness as it will be shown further on.

Going back to Experiment 1, the impact of the intermediate MoO_2 layer as part of different Mo configurations, Mo_1 and Mo_3, on the optoelectronic properties of CZTSe solar cells can be seen in **Figure 7**. **Figure 7**a shows the J-V illuminated curves of a monolayer configuration (Mo_1) and its combination with a 10 or 20 nm MoO_2 layer grown with a 30 nm Mo_A cap layer (solid lines), and the same oxide combinations with a bi-layer configuration (Mo_3, dashed lines). Additionally, a table with a summary of the main optoelectronic parameters of the cell is included. It has to be noted that none of the solar cells produced in this experimental part showed any delamination issue, usually linked with the presence of $MoSe_2$ with the c-axis perpendicular to the substrate as mentioned before. At a first glance, it is obvious that despite performing very different the CZTSe cells based on plain Mo cases, 7.3% Mo_1

and 5.7% Mo_3, after the introduction of the MoO_2 layer both cells exceed 8% when using 20 nm of MoO_2, 8.2% and 8.1% for Mo_1 and Mo_3 respectively (Mo_2 results are not shown, but they are similar to the ones based on Mo_3, going from 4.7% for the reference case to 8.1% for the 20 nm MoO_2 case). An important increase in V_{OC} and FF takes place, especially in the case of Mo_3 (about 80 mV more for V_{OC} and 7% absolute increase in FF), which is clearly responsible for the efficiency change. Moreover, the shunt resistance (R_{SH}) suffers a dramatic change as well, from 161 to 314 Ω cm^2 for Mo_1 and from 83.6 to 611 Ω cm^2 for Mo_3. It has to be noted that **Figure 7**a belongs to the best cells obtained from completed samples processed with every specific back contact type, but **Figure S8** from the S.I. shows the statistical spread for 12 cells processed in the experiment.

Figure 7b shows the spectrally resolved photocurrent collection via EQE. An increase in the whole absorption range (from 500 to 1300 nm) with the addition of a MoO_2 layer takes place correlating with the values of J_{SC} from **Figure 7**a. This fact evidences that whichever phenomena occurring in the CZTSe cells after the MoO_2 introduction take place, cannot be only correlated with a pure back contact modification. If it was the case, the EQE will only presumably have a clear impact on electrons photogenerated deeper in the absorber (800 -1300 nm) and not on all the spectral absorption range. The band gap of the different CZTSe absorbers was extracted from the energy derivative of the EQE plots and a subsequent Gaussian fit. Interestingly, for both Mo_1 and Mo_3 cases, the band gap increased after the introduction of the MoO_2 layer, reaching a maximum value for the 20 nm MoO_2 case. This fact is directly reflected in the EQE plots via a faster decrease near the band gap edge. It is significant the difference between the EQE plots of Mo_1 and Mo_3, showing a better photocurrent collection in the whole absorption range for the overselenized

monolayer compared with the almost non selenized bi-layer. This will point out again towards the necessity of controlling the thickness of $MoSe_2$ layer to avoid poor carrier collection at the CZTSe back and bulk regions.

At this stage, it seems clear that evidences arisen from the optoelectronic characterization point out towards a change in the full CZTSe absorber and not only at the back region. In order to gather more information, SEM images of full CZTSe cells based on different back contact designs were taken. **Figure 8** shows cross sectional SEM images of CZTSe solar cells based on Mo_3, Mo_3-10nmMoO_2 and Mo_3-20nmMoO_2. Additionally, SEM top view images of the CZTSe absorbers are included as insets for every image. **Figure 8**a shows a CZTSe cell with a bi-layer Mo_3 back contact, the average grain size is less than 1 μm as evidenced by the SEM cross sectional view, not reaching the full absorber thickness (~ 1.6 μm). The SEM top view inset further reveals numerous grains of several hundreds of nanometers. When the MoO_2 oxide layer is introduced an important improvement in the grain size is achieved, obtaining grains as large as the absorber thickness for both 10 and 20 nm in thickness. In the case of 20 nm thickness the length of CZTSe grains reaches values up to several microns (3-4μm), correlating with the highest performing devices. Therefore, the introduction of the MoO_2 layer has enhanced CZTSe grain growth assisting the sintering of the absorber. The bigger grain sizes also correlate with the increased values of R_{SH} after the oxide introduction, since bigger grain sizes will lead to less grain boundaries (GBs) where there could be more possibilities for carrier recombination. Nevertheless, although GBs have been proved to be positive for electronic transport in CIGS [51-53], a recent study based on a new alkali doping for CZTSSe seems to conclude the opposite [54]. Furthermore, Sardashti et al. observed this latter type of GBs behavior for CZTSSe absorbers following and oxidation,

oxygen removal and subsequent air post-annealing route, such as the one we have used in this work to produce CZTSe solar cells [55], as reported by Neuschitzer et al [56]. In consequence, GBs with an inverted potential (negatively charged) compared with what it was commonly observed for CIGS and more recently CZTSSe (positively charged GBs) [51, 57, 58], i.e. repelling minority carriers (electrons) and attracting holes would lead to a better device performance [54]. It is important to note that this would be the typical behavior that could be expected for a polycrystalline semiconductor, since GBs contain numerous defects that enhance recombination and lower devices performance.

In addition to **Figure 8**, SEM top images of CZTSe absorbers grown on the rest of back contacts analyzed in Experiment 1 are included in **Figure S9** of S.I.

It is well known that the sintering of CZTSSe is enhanced by alkali impurities, mainly Na [59-61]. Furthermore, the typical impact of alkali doping in CZTSSe performance is related with a V_{OC} and FF increase [60, 62, 63], i.e. similar to what we observed for our MoO_2 containing cells. Thus, it seems reasonable to speculate about Na diffusion modification coming from the Soda Lime Glass (no alkali barrier was used for this work) during the absorber sintering induced by the presence of the MoO_2 oxide intermediate layer. In order to confirm this hypothesis, TOF-SIMS compositional depth profiles of CZTSe full cells based on different back contacts with and without MoO_2 layers were obtained. The results are shown in **Figure S10** of the S.I. No significant variations can be drawn from the Na depth compositional profiles. Nevertheless, if the final Na profile is not significantly modified, it seems reasonable to think about a possible change of the Na diffusion process, and/or in the Na containing species involved in the sintering process. Despite we do not have any experimental proof to confirm for instance the formation of specific Na-Mo-O species

or other Na based species for the MoO_2 containing samples, we believe that at least one plausible mechanism can be suggested based on experimental findings included in relevant publications in the thin-film chalcogenide field.

First, it is important to mention that in the literature evidence of a higher Na content for CIGS with a more oxidized Mo surface can be found [64]. Moreover, Zellner et al. reported a reduction in the activation energy for Na diffusion by air annealing, supporting the idea of Na diffusion assisted by oxygen presence [65]. It has been also suggested that Mo-O species can enhance Na diffusion via solubility of Na, i.e. formation of Na containing oxides, such as $Na_2Mo_2O_4$ [66, 67]. In consequence, we can speculate with a more homogeneous distribution of Na diffusion assisted by the MoO_2 layer towards the CZTSe absorber. It is important to keep in mind that the MoO_2 is evenly covering the whole back surface and is spatially located very close to the absorber. This fact would be in contrast with the Mo-O species naturally present in the Mo back contact after sputtering, since their presence might be randomly distributed across the Mo layer. Furthermore, it is well known that Na diffuses through the Mo grain boundaries via oxygen species [38, 68, 69]. Thus, if the MoO_2 is present in a more uniform way, i.e. covering the whole Mo surface through 10 or 20 nm thick MoO_2 layers, then the Na "diffusion path" towards the absorbed might be enhanced, since the diffusion channels will not only be at the GBs, but at the whole Mo surface.

Likewise, if we take into account as it was confirmed by XRF, XRD and SEM measurements that MoO_2 acts as a selenium barrier, then the availability of Se at the bottom region of the absorber could be maximized for samples processed with MoO_2 compared with the non-MoO_2 containing ones. An improvement in the sintering of CZTSSe absorbers has been previously linked to the use of a graphite box coated with

SiO_2, a material that is also not selenized, leaving more Se available for the sintering process [70]. The effects of this coating layer could be seen as similar to the inclusion of the intermediate MoO_2 layer.

Additionally, if we accept that Na can be preferentially dissolved in the MoO_2 interfacial layer, then a combined effect of more Na available at the back interface along with more Se could be easily favoring the formation of liquid Na_2Se_x species. It should be noted that Na polyselenides have been suggested by Sutter-Fella et al, as key for CZTSSe sintering improvement due to their fluxing effect [60]. Moreover, the sticking coefficient for Na_2Se_x is higher than for Se, and thereby these compounds can significantly increase the Se availability for the absorber growth process [71].

In summary, we believe that a synergistic effect between the MoO_2 layer and the Na naturally present in the SLG could have occurred, enhancing the availability of Se possibly via beneficial Na_2Se_x liquid species during the sintering at the back CZTSe/Mo interface.

It is interesting to see as well, that in the work of Scofield et al. despite having similar Na levels for CIS absorbers (confirmed by SIMS) grown on different Mo types, the grains of the absorber were different [68]. This would be in agreement with our observations and could confirm that even when the final Na profiles in CZTSe absorbers grown on different Mo configurations are similar, the thermodynamic processes leading to these profiles seem to be more important than the final Na level themselves. We propose the MoO_2 intermediate layer as a relevant agent capable of modifying the Na diffusion thermodynamics during the absorber sintering.

To further understand the CZTSe structural changes induced by the back contact modification we decided to perform Raman spectroscopy analyses of CZTSe absorbers as part of full solar cells. The upper layers (TCO and CdS buffer) of the

cells were etched away in diluted aqueous HCl solution. The spectra obtained with a green excitation laser source (532.5 nm) are shown in **Figure 9**. It should be noted that the Raman spectra obtained belong to the first 20-50 nm of the analyzed absorbers, since Raman is a powerful surface sensitive structural characterization technique. Additionally, a summary with parameters extracted from the spectra to assess the CZTSe crystal quality and the impact of the MoO_2 layer in the absorber surface structure is included in **Table S1** of the S.I.

It can be clearly observed that the introduction of the MoO_2 has induced structural changes in the CZTSe absorbers. In particular, when focusing in Figure 9a the narrowing of the main peak confirms the increase in grain size after the introduction of the MoO_2 (see **Table S1** from S.I. for FWHM). Furthermore, the decrease in the relative intensity of peaks around the spectral region of 170 cm^{-1} when the oxide is applied, has been experimentally linked with an increase in concentration of [Zn_{Cu} + V_{Cu}] defect clusters [72]. In the case of the work of Dimitrievska et al, the changes in the Raman spectra were induced by compositional variations in the CZTSe absorbers, but in our particular case the compositional ranges are very similar (See **Table S2** of S.I.), leaving the back contact modification via MoO_2 addition as the main cause to explain the structural changes observed in CZTSe. It has to be noted that the samples were cooled down following the same temperature regime, i.e. naturally cool down to room temperature, and thereby order/disorder effects in the cation sublattice can be discarded [73-75]. In conclusion, the introduction of the MoO_2 layer induces relevant structural changes in the CZTSe absorbers confirmed by SEM and Raman spectroscopy, leading to a more depleted Cu surface since a decrease in Cu/Zn and Cu/Sn vibration units is corroborated by the Raman technique. A correlation with high performing devices and a Copper depleted surface has been already reported in

the literature [55, 56]. Before moving to the second experimental part of this work, a question that could be still pending from the results already presented would be whether the MoO_2 itself on top of the different Mo configurations without any Mo_A sacrificial cap layer could give better or similar results to the ones already shown. The answer is no, since a general degrading in all optoelectronic parameters takes place when the oxide is applied alone. Thus, the relevance of the $MoSe_2$ layer as a buffer between the CZTSe absorber and the Mo back contact is again clearly revealed as crucial for the technology. Finally, a table summarizing these results (**Table S3**), based on Mo_1 and Mo_3 configurations with different thickness of MoO_2 layers but no Mo_A cap layer (analogue to the cases analyzed by XRD in **Figure 5**) is included in the S.I.

3.2. Experiment 2: Influence of Mo Cap Layer Thickness from Mo Tri-layer Configuration and Impact of a 20 nm MoO_2 Layer in CZTSe Solar Cells

With the aim of improving further the properties of the back contact interface of our CZTSe cells, a tri-layer configuration as it was prior stated was used. The top sacrificial layer, Mo_A will allow for a fine tuning of the $MoSe_2$ layer growing between the Mo back contact and the CZTSe absorber, which we have proved to be very important to improve devices performance, in agreement with the literature [21, 50]. The objective of Experiment 2, as shown in **Figure 1**, is to study the effect of the thickness of the top layer in a tri-layer configuration and its combination with a 20 nm intermediate MoO_2 layer on CZTSe cells based on these back contacts. The role of a Mo_A layer ranging from 20 to 70 nm with and without a 20 nm underlying MoO_2 layer was investigated. **Figure 10** shows the J-V illuminated curves for the best CZTSe cells based on a tri-layer configuration (Mo_4) with and without the influence

of an intermediate MoO$_2$ layer. Again, none of the solar cells studied in this experimental part showed delamination problems.

It can be easily concluded from **Figure 10** by focusing on the green lines (tri-layer back contact configurations with different Mo$_A$ cap layers) that the thickness of the cap layer is clearly affecting the devices performance, changing all the optoelectronic parameters. **Table 4** summarizes those parameters, and an increase in efficiency from 6.2% to 7.2% was obtained when changing the cap layer from 20 to 70 nm. The photocurrent (J$_{SC}$) also experienced a remarkable increase from 29.8 to 32.7 mA/cm^2 and finally Voc and FF moderately increased as well. It is interesting to note how besides the sample with 50 nm all the parameters seem to increase in parallel with the Mo$_A$ cap layer thickness increase, and thereby we believe some processing damage could lower the performance of this particular sample. As proved before, the cap layer thickness can control the MoSe$_2$ layer thickness and therefore affect the final performance of CZTSe devices. **Table S4** of S.I. shows the MoSe$_2$ thickness values of back contacts analogue to those belonging to the CZTSe cells in green from **Figure 10** after selenization, obtained by XRF. The MoSe$_2$ thickness increases progressively from about 80 nm to 120 nm for 20 nm to 70 nm of Mo$_A$ respectively.

Focusing now on the blue lines, which belong to the same set of samples analyzed before but with an underlying 20 nm MoO$_2$ layer, a significant performance increase for all the cases (different Mo$_A$ thickness) compared with the green lines is achieved. A major increase in V$_{OC}$ and FF has boosted the efficiency up to a maximum of 9.5%. The V$_{OC}$ achieved a maximum value of 459 mV, which we believe is currently one of the highest reported for the pure selenide kesterite compound, largely exceeding the CZTSe world record device (423 mV) [76]. An absolute increase in the efficiency values of more than 2% has been possible just with the insertion of a thin MoO$_2$

intermediate layer. Again a dramatic change in R_{SH} occurs after the introduction of MoO_2 layer going from 149 to 758 Ω cm^2 for the case of 70 nm Mo_A cap layer. The statistical spread of the main optoelectronic parameters for 12 cells, besides the case based on 50 nm (due to a possible experimental damage), is shown in **Figure S11** of S.I.

It should be noted that in contrast with the results from **Figure 7**a, where the value of J_{SC} was slightly improved in all cases when introducing the MoO_2, in this case the photocurrent was slightly reduced in most of the cases. **Figure S12**a from S.I. shows the EQE plots for the cases where 30 and 70 nm Mo_A cap layer was used along with their MoO_2 based counterparts. It should be noted that other plots are not shown for reasons of simplicity. **Figure S12**b compares the J_{SC} values obtained from J-V curves and from the integration of the EQE signal over the full absorption range. The values obtained from EQE are systematically several mA/cm^2 much larger than the ones obtained from J-V for the MoO_2 containing samples. Therefore, it could be possible that when introducing the MoO_2 some light induced defects are activated under strong illumination conditions, i.e. the light from the AM1.5G standard conditions of our solar simulator. As a result, the current collection is reduced under these illumination conditions, being notably increased when illuminating via monochromatic light from EQE.

Although the best results have been obtained using a Mo multilayered structure combined with MoO_2, it is important to take into consideration that the Mo tri-layer configuration (Mo_4) that we have defined offers a wide range in terms of optimization/usage. Recent results using this type of back contact layout but changing the thickness of the Mo_A and Mo_B constituent layers allowed us to increase the efficiency from 7.2 to 8.9% as it can be observed in **Figure 11**. It can be easily

noticed how by increasing the amount of the bottom Mo_A with regard to Mo_B a remarkable increase in CZTSe cell performance was possible. The effect is mainly due to an increase in V_{OC}, FF and Rsh. We believe by further tuning of this configuration and with MoO_2, higher CZTSe devices performance can be achieved.

In summary, in this work we reported on the crucial relevance of the back contact interface for CZTSe cells performance. Multilayered Mo configurations seem to be necessary to avoid overselenization of the back contact and to control the thickness of the $MoSe_2$, which we have demonstrated to clearly affect devices performance. Furthermore, we introduced for the first time a thin MoO_2 layer as part of the back contact design, significantly improving CZTSe cells efficiency via FF but also V_{OC}, a critical parameter currently hindering the ambitioned kesterite future progress and commercialization. The improvement of the optoelectronic parameters of CZTSe devices correlates with relevant CZTSe absorber morphological and structural changes, not limiting the effects of this oxide layer to the back contact region.

4. Conclusion

We have developed a Mo multilayer configuration capable of dealing with one of the most relevant issues of CZTSSe technology, overselenization of the back region with the subsequent absorber decomposition and reduction of devices performance. A tri-layer configuration has been designed in order to deal with this problem, but also to efficiently tune the thickness of the $MoSe_2$ directly in contact with the CZTSe absorber. The thickness of a top sacrificial Mo_A cap layer is the parameter that allows for $MoSe_2$ thickness control. By modifying its thickness, optoelectronic parameters such as FF and V_{OC} can be increased. Additionally, we introduced for the first time a thin intermediate MoO_2 layer as part of several Mo configurations in CZTSSe technology. This layer acts as an efficient barrier against selenization. Moreover, it

causes a texture change in the $MoSe_2$ layer growing in contact, inducing its growth with the c-axis perpendicular to the substrate. A correlation of the amount of $MoSe_2$ with the Se-Mo-Se sheets growing parallel to the Mo substrate and the MoO_2 layer thickness can be established. Additionally, a major efficiency increase regardless the type of Mo configuration chosen has been obtained when using a 20 nm MoO_2 layer. Up to more than 2% absolute increase was possible reaching a maximum efficiency of 9.5%. An important increase in FF but also in V_{OC}, a crucial parameter for CZTSSe technology has been obtained. A CZTSe solar cell with 459 mV of V_{OC} has been produced. This is one of the highest values reported for the technology. In addition, the MoO_2 layer assists CZTSe sintering allowing for much larger grains when the oxide is applied. Furthermore, a significant increase in R_{SH} resistance lies in parallel with the observed grain size increase. In summary, the introduction of this layer could set a viable route to explore for CZTSSe technology in order to deal with the severe voltage deficit that currently is hindering its progress.

5. Acknowledgements

6. References

[1]   W. Wang, M. T. Winkler, O. Gunawan, T. Gokmen, T. K. Todorov, Y. Zhu, D. B. Mitzi, Adv. Energy Mater. 4 (2013) 1301465.

[2]   T. J. Huang, X. Yin, G. Qi, H. Gong, Phys. Status Solidi RRL. 08 (2014) 735-762.

[3]   A. Polizzotti, I. L. Repins, R. Noufi, S.-H. Wei, D. B. Mitzi, Energy Environ. Sci. 6 (2013) 3171-3182.

[4]   I. L. Repins, M. J. Romero, J. V. Li, W. Su-Huai, D. Kuciauskas, J. Chun-Sheng, C. Beall, C. DeHart, J. Mann, H. Wan-Ching, G. Teeter, A. Goodrich, R. Noufi, Photovoltaics, IEEE Journal of. 3 (2012) 439-445.

[5]   S. Siebentritt, Thin Solid Films. 535 (2013) 1-4.

[6]   S. Siebentritt, S. Schorr, Prog. Photovol: Res. Appl. 20 (2012) 512-519.

[7]   I. Repins, N. Vora, C. Beall, S.-H. Wei, Y. Yan, M. Romero, G. Teeter, H. Du, B. To, M. Young, R. Noufi, MRS Online Proc. Libr. 1324 (2011).

[8]   I. V. Dudchak, L. V. Piskach, J. Alloys Compd. 351 (2003) 145-150.

[9]   I. D. Olekseyuk, I. V. Dudchak, L. V. Piskach, J. Alloys Compd. 368 (2004) 135-143.

[10]   J. J. Scragg, P. J. Dale, D. Colombara, L. M. Peter, ChemPhysChem. 13 (2012) 3035-3046.

[11] T. Gershon, B. Shin, T. Gokmen, S. Lu, N. Bojarczuk, S. Guha, Appl. Phys. Lett. 2013, 103 193903.

[12] T. Gokmen, O. Gunawan, T. K. Todorov, D. B. Mitzi, Appl. Phys. Lett. 103 (2013) 103506.

[13] J. Krustok, R. Josepson, T. Raadik, M. Danilson, Phys. B. 405 (2010) 3186-3189.

[14] S. Oueslati, G. Brammertz, M. Buffière, C. Köble, T. Oualid, M. Meuris, J. Poortmans, Sol. Energy Mater. Sol. Cells. 134 (2015) 340-345.

[15] A. Fairbrother, E. García-Hemme, V. Izquierdo-Roca, X. Fontané, F. A. Pulgarín-Agudelo, O. Vigil-Galán, A. Pérez-Rodríguez, E. Saucedo, J. Am. Chem. Soc. 134 (2012) 8018-8021.

[16] S. López-Marino, Y. Sánchez, M. Placidi, A. Fairbrother, M. Espindola-Rodríguez, X. Fontané, V. Izquierdo-Roca, J. López-García, L. Calvo-Barrio, A. Pérez-Rodríguez, E. Saucedo, Chem. - Eur. J. 19 (2013) 14814-14822.

[17] M. Mousel, A. Redinger, R. Djemour, M. Arasimowicz, N. Valle, P. Dale, S. Siebentritt, Thin Solid Films. 535 (2013) 83-87.

[18] H. Xie, Y. Sánchez, S. López-Marino, M. Espíndola-Rodríguez, M. Neuschitzer, D. Sylla, A. Fairbrother, V. Izquierdo-Roca, A. Pérez-Rodríguez, E. Saucedo, ACS Appl. Mater. Interfaces. 6 (2014) 12744-12751.

[19] S. Lopez-Marino, M. Placidi, A. Perez-Tomas, J. Llobet, V. Izquierdo-Roca, X. Fontane, A. Fairbrother, M. Espindola-Rodriguez, D. Sylla, A. Perez-Rodriguez, E. Saucedo, J. Mater. Chem. A. 1 (2013) 8338-8343.

[20] S. Oueslati, G. Brammertz, M. Buffière, H. ElAnzeery, D. Mangin, O. ElDaif, O. Touayar, C. Köble, M. Meuris, J. Poortmans, J. Phys. D: Appl. Phys. 48 (2015) 035103.

[21]   B. Shin, Y. Zhu, N. A. Bojarczuk, S. J. Chey, S. Guha, Appl. Phys. Lett. 101 (2012) 053903.

[22]   J. J. Scragg, J. T. Wätjen, M. Edoff, T. Ericson, T. Kubart, C. Platzer-Björkman, J. Am. Chem. Soc. 134 (2012) 19330-19333.

[23]   M. Buffière, G. Brammertz, M. Batuk, C. Verbist, D. Mangin, C. Koble, J. Hadermann, M. Meuris, J. Poortmans, Appl. Phys. Lett., 105 (2014) 183903.

[24]   W. Takahiro, K. Naoki, N. Takayuki, N. Mikihiko, Jpn. J. Appl. Phys. 35 (1996) L1253.

[25]   T. Wada, N. Kohara, S. Nishiwaki, T. Negami, Thin Solid Films. 387 (2001) 118-122.

[26]   W. N. Shafarman, J. E. Phillips, Conf. Rec, Twenty Fith IEEE Photovoltaic Spec. Conf. (1996) 917-919.

[27]   F. Liu, K. Sun, W. Li, C. Yan, H. Cui, L. Jiang, X. Hao, M. A. Green, Appl. Phys. Lett. 104 (2014) 051105.

[28]   H. Cui, C.-Y. Lee, W. Li, X. Liu, X. Wen, X. Hao, Int. J. Photoenergy. 2015 (2015) 9.

[29]   P. M. P. Salomé, V. Fjallstrom, A. Hultqvist, P. Szaniawski, U. Zimmermann, M. Edoff, *Prog.* Photovolt.: Res. Appl. 22 (2014) 83-89.

[30]   K.-J. Yang, J.-H. Sim, B. Jeon, D.-H. Son, D.-H. Kim, S.-J. Sung, D.-K. Hwang, S. Song, D. B. Khadka, J. Kim, J.-K. Kang, Prog. Photovolt.: Res. Appl. 23 (2014) 862.

[31]   C. Leidholm, C. Hotz, A. Breeze, C. Sunderland, W. Ki, D. Zehnder, NREL Report No. NREL/SR-5200-56501. (2012).

[32]   A. Duchatelet, G. Savidand, R. N. Vannier, D. Lincot, Thin Solid Films. 545 (2013) 94-99.

[33]   M. Neuschitzer, Y. Sanchez, S. López-Marino, H. Xie, A. Fairbrother, M. Placidi, S. Haass, V. Izquierdo-Roca, A. Perez-Rodriguez, E. Saucedo, Prog. Photovolt.: Res. Appl. (2015) DOI: 10.1002/pip.2589.

[34]   A. Fairbrother, X. Fontané, V. Izquierdo-Roca, M. Placidi, D. Sylla, M. Espindola-Rodriguez, S. López-Mariño, F. A. Pulgarín, O. Vigil-Galán, A. Pérez-Rodríguez, E. Saucedo, Prog. Photovolt.: Res. Appl. 22 (2014) 479-487.

[35]   J. H. Scofield, A. Duda, D. Albin, B. L. Ballard, P. K. Predecki, Thin Solid Films. 260 (1995) 26-31.

[36]   C. Roger, S. Noël, O. Sicardy, P. Faucherand, L. Grenet, N. Karst, H. Fournier, F. Roux, F. Ducroquet, A. Brioude, S. Perraud, Thin Solid Films. 548 (2013) 608-616.

[37]   P. M. P. Salomé, J. Malaquias, P. A. Fernandes, A. F. d. Cunha, J. Phys. D: Appl. Phys. 43 (2010) 345501.

[38]   P. Blösch, S. Nishiwaki, L. Kranz, C. M. Fella, F. Pianezzi, T. Jäger, C. Adelhelm, E. Franzke, S. Buecheler, A. N. Tiwari, Sol. Energy Mater. Sol. Cells. 124 (2014) 10-16.

[39]   K.-H. Müller, J. Appl. Phys. 62 (1987) 1796-1799.

[40]   T. J. Vink, M. A. J. Somers, J. L. C. Daams, A. G. Dirks, J. Appl. Phys. 70 (1991) 4301-4308.

[41]   W. H. McCarroll, K. V. Ramanujachary, Encyclopedia of Inorganic Chemistry, John Wiley & Sons, Ltd, 2006.

[42]   D. Abou-Ras, G. Kostorz, D. Bremaud, M. Kälin, F. V. Kurdesau, A. N. Tiwari, M. Döbeli, Thin Solid Films. 480-481 (2005) 433-438.

[43]   M. K. Agarwal, L. T. Talele, Mater. Res. Bull. 20 (1985) 329-336.

[44]   A. Jäger-Waldau, M. C. Lux-Steiner, E. Bucher, L. Scandella, A. Schumacher, R. Prins, Appl. Surf. Sci. 65-66 (1993) 465-472.

[45] D. Abou-Ras, D. Mukherji, G. Kostorz, D. Bremaud, M. Kälin, D. Rudmann, M. Döbeli, A. N. Tiwari, MRS Online Proc. Lib. 865 (2005) F8.1.

[46] Shiro Nishiwaki, Naoki Kohara, Takayuki Negami, Takahiro Wada, Japanese Jpn. J. Appl. Phys. 37 (1998) L71.

[47] J. A. Wilson, A. D. Yoffe, Adv. Phys. 18 (1969) 193-335.

[48] R. Würz, D. Fuertes Marrón, A. Meeder, A. Rumberg, S. M. Babu, T. Schedel-Niedrig, U. Bloeck, P. Schubert-Bischoff, M. C. Lux-Steiner, Thin Solid Films. 431-432 (2003) 398-402.

[49] J.-H. Yoon, J.-H. Kim, W. M. Kim, J.-K. Park, Y.-J. Baik, T.-Y. Seong, J.-h. Jeong, Prog. Photovolt.: Res. Appl. 22 (2013) 90-96.

[50] J. Li, Y. Zhang, W. Zhao, D. Nam, H. Cheong, L. Wu, Z. Zhou, Y. Sun, Adv. Energy Mater. 5 (2015) 1402178.

[51] C. S. Jiang, R. Noufi, K. Ramanathan, J. A. AbuShama, H. R. Moutinho, M. M. Al-Jassim, Appl. Phys. Lett. 85 (2004) 2625-2627.

[52] C. S. Jiang, M. A. Contreras, I. Repins, H. R. Moutinho, Y. Yan, M. J. Romero, L. M. Mansfield, R. Noufi, M. M. Al-Jassim, Appl. Phys. Lett. 101 (2012) 033903.

[53] S. Siebentritt, M. Igalson, C. Persson, S. Lany, Prog. Photovolt.: Res. Appl. 18 (2010) 390-410.

[54] H. Xin, S. M. Vorpahl, A. D. Collord, I. L. Braly, A. R. Uhl, B. W. Krueger, D. S. Ginger, H. W. Hillhouse, Phys. Chem. Chem. Phys. (2015) DOI 10.1039/c5cp04707b.

[55] K. Sardashti, R. Haight, T. Gokmen, W. Wang, L.-Y. Chang, D. B. Mitzi, A. C. Kummel, Adv. Energy Mater. 5 (2015) 1402180.

[56]   M. Neuschitzer, Y. Sanchez, T. Olar, T. Thersleff, S. Lopez-Marino, F. Oliva, M. Espindola-Rodriguez, H. Xie, M. Placidi, V. Izquierdo-Roca, I. Lauermann, K. Leifer, A. Perez-Rodriguez, E. Saucedo, Chem. Mater. 27 (2015) 5279-5287.

[57]   J. B. Li, V. Chawla, B. M. Clemens, Adv. Mater. 24 (2012) 720-723.

[58]   C. S. Jiang, I. L. Repins, C. Beall, H. R. Moutinho, K. Ramanathan, M. M. Al-Jassim, Sol. Energy Mater. Sol. Cells. 132 (2015) 342-347.

[59]   T. Gershon, B. Shin, N. Bojarczuk, M. Hopstaken, D. B. Mitzi, S. Guha, Adv. Energy Mater. 5 (2014) 1400849.

[60]   C. M. Sutter-Fella, J. A. Stückelberger, H. Hagendorfer, F. La Mattina, L. Kranz, S. Nishiwaki, A. R. Uhl, Y. E. Romanyuk, A. N. Tiwari, Chem. Mater. 26 (2014) 1420-1425.

[61]   W. M. Hlaing Oo, J. L. Johnson, A. Bhatia, E. A. Lund, M. M. Nowell, M. A. Scarpulla, J. Electron. Mater. 40 (2011) 2214-2221.

[62]   J. V. Li, D. Kuciauskas, M. R. Young, I. L. Repins, Appl. Phys. Lett. 102 (2013) 163905.

[63]   S. López-Marino , Y. Sánchez , M. Espíndola-Rodríguez, X. Alcobé , H. Xie, M. Neuschitzer, I. Becerril , S. Giraldo , M. Dimitrievska , M. Placidi , L. Fourdinier, V. Izquierdo-Roca , A. Pérez-Rodríguez, Edgardo Saucedo, J. Mater. Chem. A. 4 (2016) 1895-1907.

[64]   J.-H. Yoon, T.-Y. Seong, J.-h. Jeong, Progress in Photovoltaics: Research and Applications 21 (2013) 58-63.

[65]   M. B. Zellner, R. W. Birkmire, E. Eser, W. N. Shafarman, J. G. Chen, Prog. Photovolt.: Res. Appl. 11 (2003) 543-548.

[66]   B. M. Basol, V. K. Kapur, C. R. Leidholm, A. Minnick, A. Halani, Conf. Rec, Twenty Fourth IEEE Photovoltaic Spec. Conf. 1 (1994) 148-151.

[67] M. Ruckh, D. Schmid, M. Kaiser, R. Schaffler, T. Walter, H. W. Schock, Conf. Rec, Twenty Fourth IEEE Photovoltaic Spec. Conf. 1 (1994) 156-159.

[68] J. H. Scofield, S. Asher, D. Albin, J. Tuttle, M. Contreras, D. Niles, R. Reedy, A. Tennant, R. Noufi, Conf. Rec, Twenty Fourth IEEE Photovoltaic Spec. Conf. 1 (1994) 164-167.

[69] M. Bodegard, K. Granath, L. Stolt, A. Rockett, Sol. Energy Mater. Sol. Cells. 58 (1999) 199-208.

[70] S. G. Haass, M. Diethelm, M. Werner, B. Bissig, Y. E. Romanyuk, A. N. Tiwari, Adv. Energy Mater. 5 (2015) 1500712.

[71] D. Braunger, D. Hariskos, G. Bilger, U. Rau, H. W. Schock, Thin Solid Films 361-362 (2000) 161.

[72] M. Dimitrievska, A. Fairbrother, E. Saucedo, A. Pérez-Rodríguez, V. Izquierdo-Roca, Appl. Phys. Lett. 106 (2015) 073903.

[73] G. Rey, A. Redinger, J. Sendler, T. P. Weiss, M. Thevenin, M. Guennou, B. El Adib, S. Siebentritt, Appl. Phys. Lett. 105 (2014) 112106.

[74] J. J. S. Scragg, L. Choubrac, A. Lafond, T. Ericson, C. Platzer-Björkman, Appl. Phys. Lett. 104 (2014) 041911.

[75] S. Schorr, Sol. Energy Mater. Sol. Cells, 95 (2011) 1482-1488.

[76] Y. S. Lee, T. Gershon, O. Gunawan, T. K. Todorov, T. Gokmen, Y. Virgus, S. Guha, Adv. Energy Mater. 5 (2014) 1401372.

7. Vitae

Simón López-Marino holds M.S. degrees in chemical engineering from the University of Santiago de Compostela (USC), Spain, and in renewable energy with specialization in photovoltaics from the Universities of Zaragoza and Northumbria, Spain and UK. He recently received his Ph.D. degree in materials science from the Polytechnic University of Catalonia (UPC). His doctoral work focused on CZTSe solar cells and was fully developed at the Catalonia Institute for Energy Research (IREC). He is now part of the Estonian-Austrian photovoltaic company Crystalsol. His research interests are characterization and development of thin film chalcogenide solar cells on SLG and alternative and flexible substrates.

Moises Espíndola-Rodriguez is a postdoctoral research fellow at the Catalonia Institute for Energy Research (IREC). He received his Ph.D. in Engineering and Advanced Technologies from Department of Physics, Barcelona University, Spain in 2015. His research interest focuses on device engineering, synthesis and optoelectronic characterization of Perovskite and CZTSSe thin film solar cells.

Yudania Sánchez holds an M.S. degree in inorganic chemistry from the Department of Chemistry of the University of La Habana, Cuba. She received her Ph.D. degree from the Department of Physics, University of Barcelona, Spain in 2016. Now she is a Research Associate at Catalonia Institute for Energy Research (IREC), Spain. Her research interests are the development of low-cost deposition techniques such as spray pyrolysis and chemical bath deposition (CBD) for thin film chalcogenide based solar cells. She is particularly interested in the investigation of alternative buffers to replace the conventional CdS layer.

Xavier Alcobé is a scientist at the University of Barcelona (UB). He is the X-Ray Diffraction Unit manager of the Scientific and Technological Centers of UB since 1988, an institute dedicated to give research support and assessment to the scientific community. He received his Ph.D. degree in Crystallography from the UB in 2007. He has published numerous scientific papers, all of them including work in X-ray powder diffraction, especially in phase analysis and structural characterization by full profile analysis. Recently he joined research teams in photovoltaics, collaborating in the structural characterization of the related materials.

Florian Oliva obtained his M.S. degree in Material Science from Montpellier University (France) in 2010 and started an industrial Ph.D. degree in Nexcis company (France) the same year on the optimization of annealing treatments in electrodeposition-based CIGSSe manufacturing. After successfully defending his Ph.D. degree in 2014, he obtained a postdoctoral position in IREC (Spain) in the framework of several European projects. His research interests include manufacturing of CZTS and CIGS based thin-film solar cells and their characterization especially by Raman spectroscopy and photoluminescence technique.
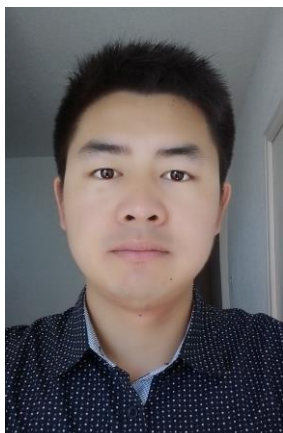
Haibing Xie received his M.S. degree from department of chemistry and materials, University of Science and Technology of China, in 2012. Now he is a Ph.D. student at Catalonia Institute for Energy Research (IREC), Barcelona, Spain. His current research interests focus on the development of CZTSSe thin film solar cells based on a single-step sulfo-selenization methodology.

Markus Neuschitzer received his M.S. degree in Technical Physics from Graz University of Technology, Austria, in 2012. During his Master's thesis, carried out at the Institute of Solid State Physics in Graz, Austria, he worked on X-ray based thin film characterization techniques for organic electronics and heterojunction solar cells. In 2013 he joined the Catalonia Institute for Energy Research in Barcelona, Spain, as a Marie Curie early stage researcher in the framework of the ITN KESTCELLS (www.kestcells.eu) and is currently working towards his Ph.D. degree with the focus on synthesis of kesterite absorbers by PVD processes and front interface optimization.

Sergio Giraldo is a Ph.D. student at Department of Advanced Materials for Energy, Catalonia Institute for Energy Research (IREC), Barcelona, Spain. After obtaining the master's degree, he focused his career on sustainable photovoltaic technologies, using earth abundant elements. He was awarded a FPI fellowship from the Spanish Ministry, starting the Ph.D. thesis under the supervision of Dr. Edgardo Saucedo and Prof. Alejandro Pérez-Rodríguez. His current research focuses on developing new strategies for improving kesterite devices performance.

Marcel Placidi obtained his Ph.D. degree in 2010 at the Centro Nacional de Microelectrónica de Barcelona (CNM). His Ph.D. work was devoted to the study of wide band gap semiconductors (such as SiC and GaN) for MEMS and related process technologies. He is currently working at Institut de Recerca en Energia de Catalunya (IREC) on thin film photovoltaics, mainly with kesterite and chalcopyrite materials. Marcel has authored more than 70 papers in high impact factor journals (impact factor of 16), supervised 1 Ph.D. thesis and been involved in more than 10 European and Spanish projects.

Raquel Caballero received the degree in physics in 1998 from Granada University, Spain, and the Ph.D. degree in 2004 from the University Autonoma of Madrid (UAM), Spain. During 2004–2006 she was a postdoctoral researcher with Hahn-Meitner Institut, Berlin, Germany. From 2007 to July 2011, she was a scientist with the HZB. Currently, she is a scientist with the Applied Physic Department, UAM. Her research work is focused on chalcopyrite and kesterite thin films for solar cells. Dr. Caballero has 93 recorded articles (h-index = 25), is co-author of a book chapter and she has been involved in 15 projects.

Victor Izquierdo-Roca obtained his Ph.D. degree in Physical Sciences at the University of Barcelona, 2011. In 2012, he obtained a 'Juan de la Cierva' fellowship in Material Science and Technology. Actually he is coordinator of the characterization unit in the Solar Energy Materials and Systems Group at IREC institute. His work is focused on the development of Raman spectroscopy for fundamental characterization of PV materials and development of optical methodologies suitable for industrial processes quality control. He is coauthor of 100 papers (h factor 23), 2 patents, and he has supervised 3 Ph.D. thesis.

Alejandro Pérez-Rodríguez (Physics degree 1984, Ph.D. degree 1987) is Full Professor in the Department of Electronics of the University of Barcelona. Since February 2009 he is ascribed to the Catalonia Institute for Energy Research (IREC) as Head of the Solar Energy Materials and Systems. His research interests include the advanced characterization of processes for cost efficient thin film photovoltaic technologies.

Edgardo Saucedo obtained his Ph.D. degree in Materials Physics at the Universidad Autónoma de Madrid, Spain. In 2007, he joined IRDEP (Paris, France), and he has more than three year postdoctoral experience in France. Currently, he is the responsible of the Solar Energy Materials and Systems laboratory at IREC (Barcelona, Spain). He holds three patents and has authored more than 135 papers in high impact factor journals (h-index of 25). He has been involved in more than 15 European and Spanish Projects and is the coordinator of the ITN Marie Curie network Kestcell (www.kestcells.eu). He has supervised 6 Ph.D. thesis.

Table 1. Sputtering deposition conditions for the Mo layers involved in the back contact configurations subject of this study.

Layer	Power (W/cm^2)	Pressure (mbar)	Temperature (°C)
Mo$_A$	4.2	1.3x10^{-3}	RT$^{a)}$
Mo$_{A'}$	4,2	3x10^{-3}	RT
Mo$_B$	2,8	5x10^{-3}	RT

$^{a)}$Room Temperature

Table 2. Summary of the different back contact configurations (sample name, layer configuration, layer thickness and sheet resistance).

Sample name	Layer configuration	Thickness (nm)	Sheet resistance (Ω/sq)
Mo$_1$	Mo$_A$	800	0.22
Mo$_1$-10MoO$_2$	Mo$_A$+MoO$_2$+Mo$_A$	800+10+30	0.22
Mo$_1$-20MoO$_2$	Mo$_A$+MoO$_2$+Mo$_A$	800+20+30	0.22
Mo$_2$	Mo$_{A'}$+Mo$_B$	150+500	1.00
Mo$_2$-10MoO$_2$	Mo$_{A'}$+Mo$_B$+MoO$_2$+Mo$_A$	150+500+10+30	1.06
Mo$_2$-20MoO$_2$	Mo$_{A'}$+Mo$_B$+MoO$_2$+Mo$_A$	150+500+20+30	1.06
Mo$_3$	Mo$_A$+Mo$_B$	150+500	0.80
Mo$_3$-10MoO$_2$	Mo$_A$+Mo$_B$+MoO$_2$+Mo$_A$	150+500+10+30	0.79
Mo$_3$-20MoO$_2$	Mo$_A$+Mo$_B$+MoO$_2$+Mo$_A$	150+500+20+30	0.77
Mo$_4$	Mo$_A$+Mo$_B$+Mo$_A$	250+500+(20,30,50,70)	0.58-0.60
Mo$_4$-20MoO$_2$	Mo$_A$+Mo$_B$+MoO$_2$+Mo$_A$	250+500+20+(20,30,50,70)	0.60-0.61

Table 3. XRF estimated values for the thickness of a MoSe$_2$ layer formed after the selenization of different Mo configurations, and Mo layer thickness remaining after the same annealing process. Note all the Mo configurations with MoO$_2$ have a 30 nm sacrificial Mo$_A$ top layer.

Sample name	MoSe$_2$ (nm)	Remaining Mo (nm)
Mo$_1$	688	542
Mo$_1$-10MoO$_2$	255	622
Mo$_1$-20MoO$_2$	240	649
Mo$_2$	84	560
Mo$_2$-10MoO$_2$	174	571
Mo$_2$-20MoO$_2$	140	589
Mo$_3$	75	560
Mo$_3$-10MoO$_2$	155	596
Mo$_3$-20MoO$_2$	174	567

Table 4. Summary of optoelectronic parameters from CZTSe solar cells of Figure 10.

Mo types	J_{SC} (mA/cm^2)	V_{OC} (mV)	FF (%)	η (%)	R_s (Ω cm^2)	R_{sh} (Ω cm^2)
Mo$_4$ (20 nm Mo$_A$)	29.8	380	54.7	6.2	0.72	83
Mo$_4$ (30 nm Mo$_A$)	31.1	391	55.5	6.7	0.50	174
Mo$_4$ (50 nm Mo$_A$)	29.4	354	57.6	6.0	0.57	145
Mo$_4$ (70 nm Mo$_A$)	32.7	392	56.4	7.2	0.65	149
Mo$_4$-20MoO$_2$ (20 nm Mo$_A$)	31.1	400	65.8	8.2	0.57	400
Mo$_4$-20MoO$_2$ (30 nm Mo$_A$)	31.0	406	64.1	8.1	0.78	338
Mo$_4$-20MoO$_2$ (50 nm Mo$_A$)	29.1	400	62.6	7.3	0.54	184
Mo$_4$-20MoO$_2$ (70 nm Mo$_A$)	31.6	459	65.9	9.5	0.60	738
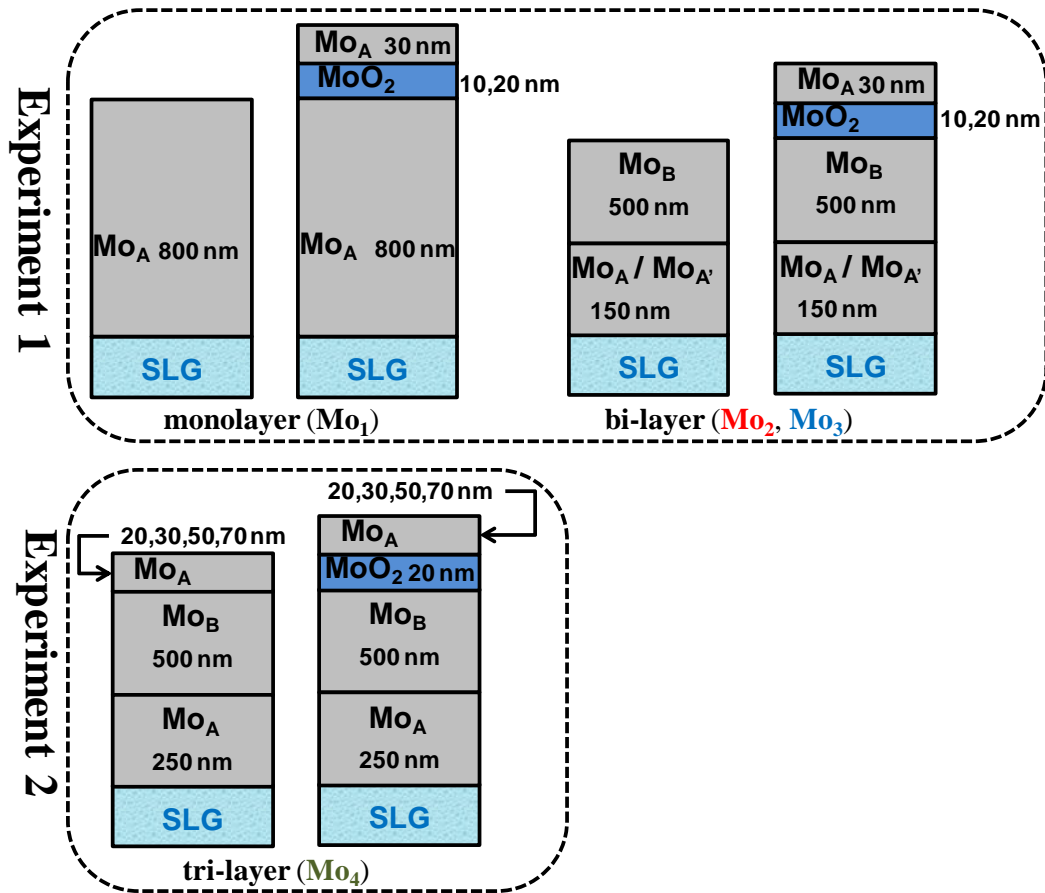
Figure 1. Graphical summary of the different back contact designs for experiment 1 and 2. Experiment 1: Comparison between Mo monolayer (Mo_1) and Mo bi-layers (Mo_2, Mo_3) and influence of an intermediate MoO_2 layer (10, 20 nm). Experiment 2: Influence of the thickness of a Mo_A cap layer in a tri-layer configuration and impact of the introduction of a 20 nm MoO_2 layer in this configuration. Note that a 10 nm i-ZnO layer has also been added on top of all these configurations, as explained in section 2, but it is not shown for simplicity reasons.
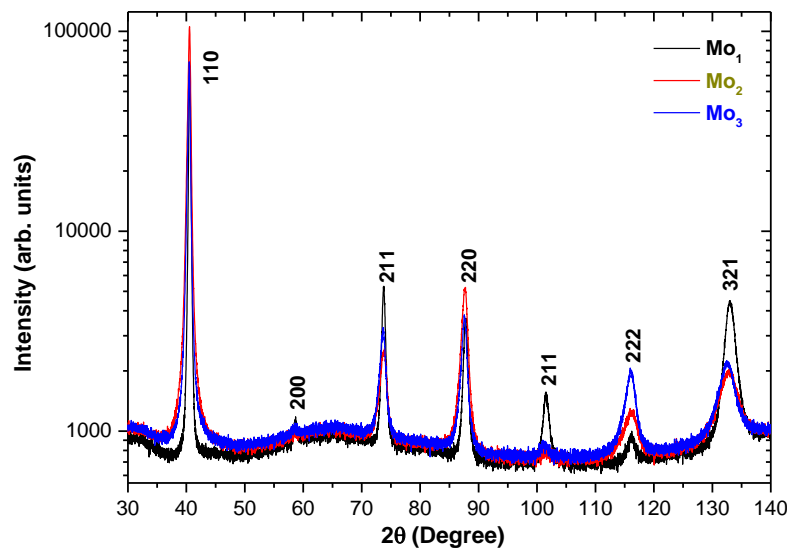
Figure 2. XRD patterns from monolayer (Mo_1) and bi-layers (Mo_2, Mo_3) back contact configurations. Relevant structural differences can be noticed.
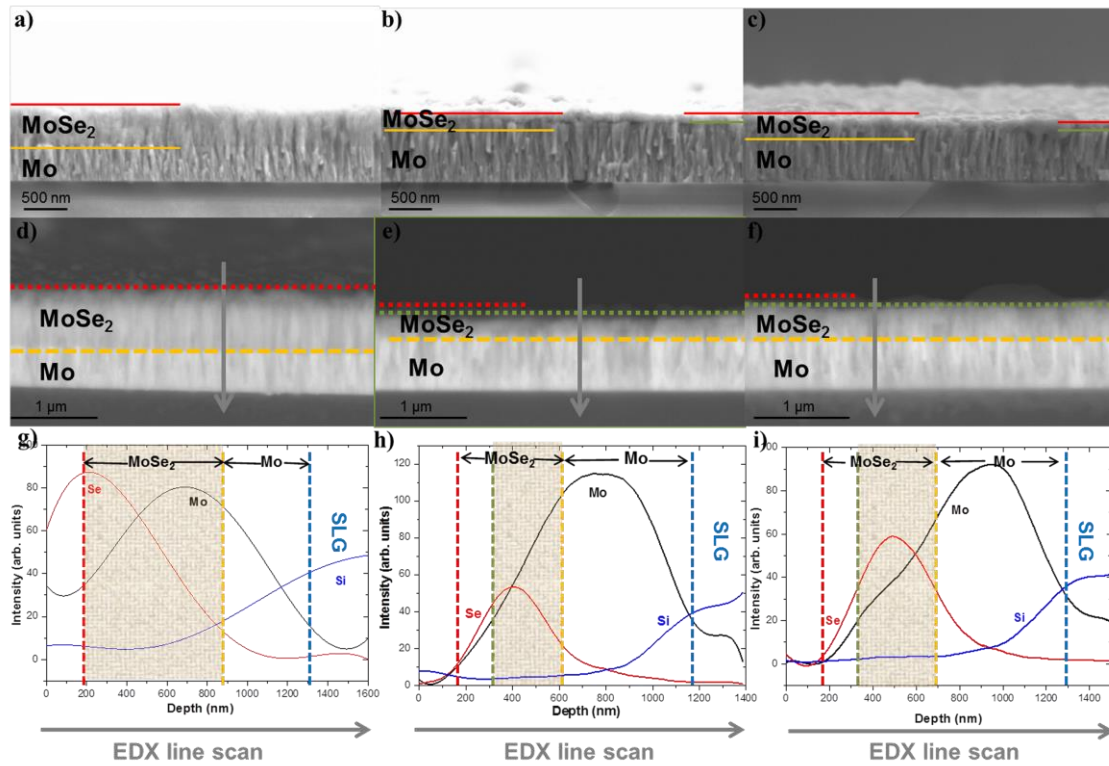
Figure 3. Cross sectional SEM and elemental depth profiles from EDX line scan images of samples Mo_1, Mo_1-10MoO_2 and Mo_1-20MoO_2 after selenization; a), b) and c): Secondary electrons detector images for selenized Mo_1, Mo_1-10MoO_2 and Mo_1-20MoO_2 respectively; d), e) and f): back scattered electrons detector images for selenized Mo_1, Mo_1-10MoO_2 and Mo_1-20MoO_2; g), h) and i): EDX line scan elemental depth profile of selenized Mo_1, Mo_1-10MoO_2 and Mo_1-20MoO_2 respectively.
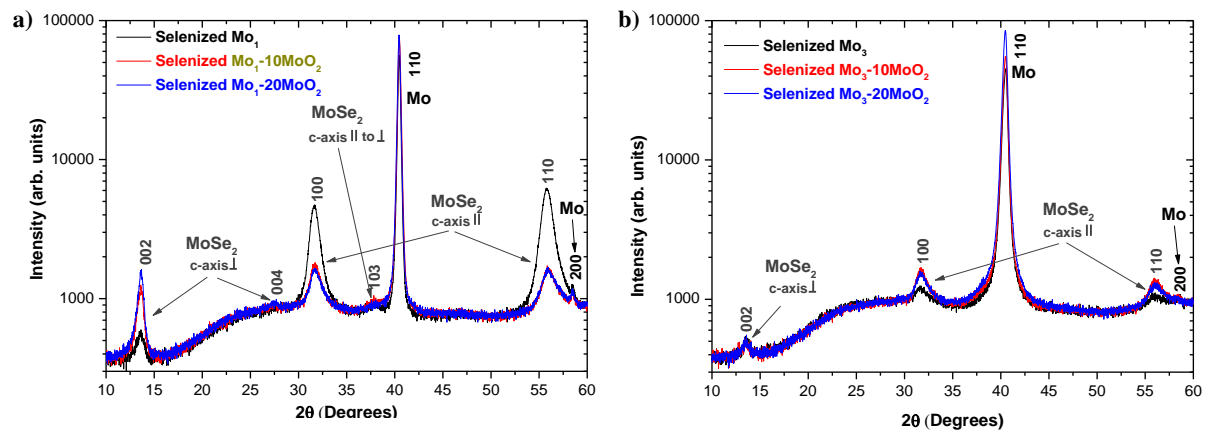
Figure 4. XRD patterns of different back contact configurations; a) Mo_1, Mo_1-10MoO_2 and Mo1-20MoO_2; b) Mo_3, Mo_3-10MoO_2 and Mo_3-20MoO_2. Different crystalline orientations can be noticed for $MoSe_2$ due to changes in the c-axis

orientation. Note that the MoO_2 layer was combined with a sacrificial 30 nm Mo_A cap layer.
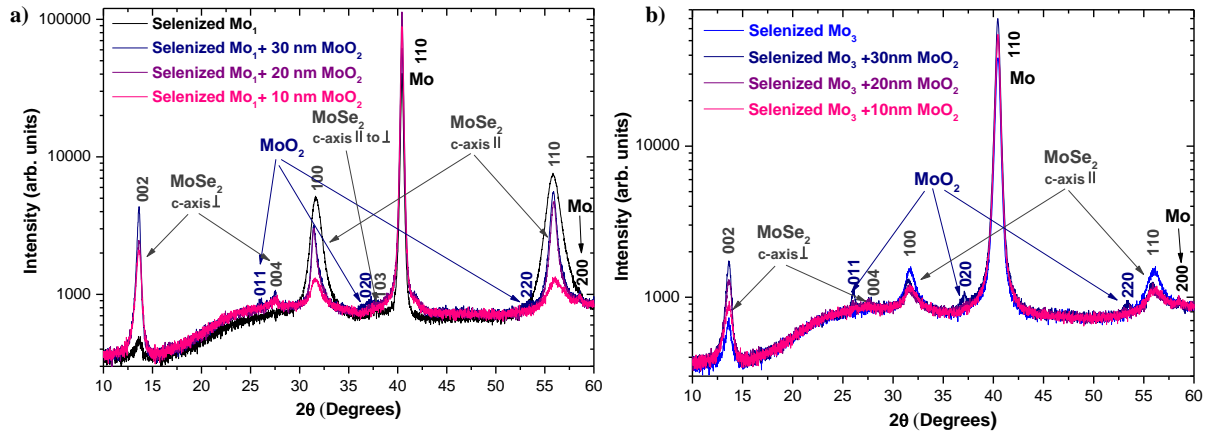
Figure 5. XRD patterns of monolayer and bi-layer configurations with different MoO_2 layers grown on top of them (No Mo_A cap layer); a) Mo_1 with 10, 20 and 30 nm of MoO_2 layer; b) Mo_3 with 10, 20 and 30 nm of MoO_2 on top.
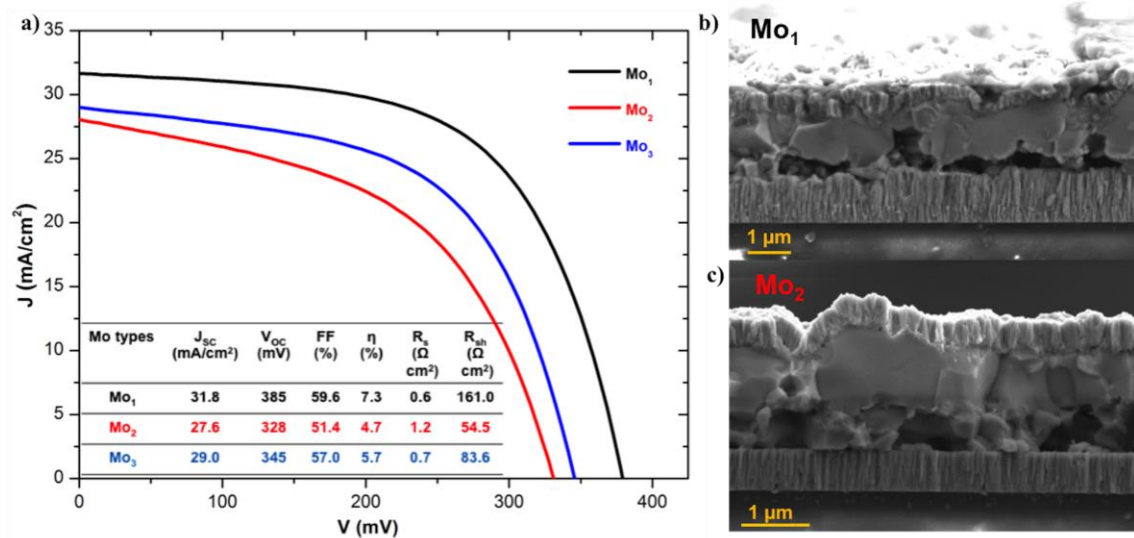
Figure 6. a) J-V illuminated curves of CZTSe with Mo_1, Mo_2 and Mo_3 back contacts; b) SEM cross sectional image of full CZTSe solar cells based on Mo_1 and Mo_2 back contacts (Note that the CZTSe cell based on Mo_3 has similar features than the Mo_2 one).
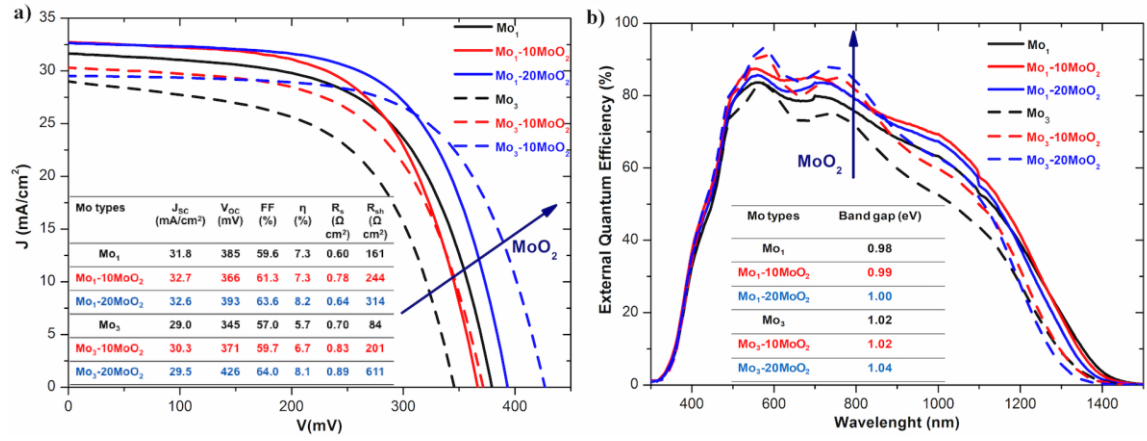
Figure 7. J-V illuminated curves and EQE of CZTSe solar cells with different back contact configurations with and without MoO_2. a) I-V illuminated curves of CZTSe with Mo_1, Mo_1-$10MoO_2$, Mo_1-$20MoO_2$, Mo_3, Mo_3-$10MoO_2$ and Mo_3-$20MoO_2$ back contacts. b) EQE of CZTSe solar cells based on Mo_1 Mo_1-$10MoO_2$, Mo_1-$20MoO_2$, Mo_3, Mo_3-$10MoO_2$ and Mo_3-$20MoO_2$ back contacts. (Note that the results of the CZTSe cell based on Mo_2 are similar to the ones based on Mo_3).
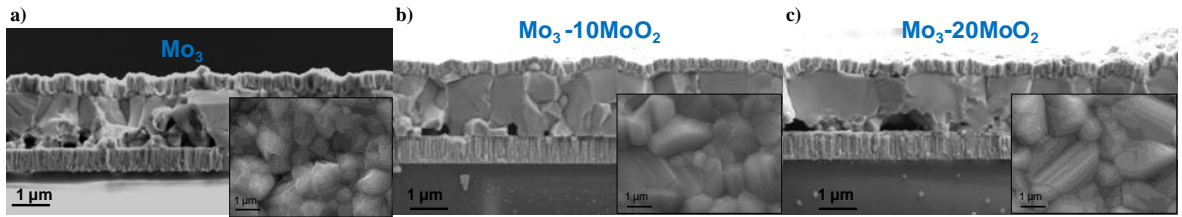
Figure 8. Cross sectional SEM images of CZTSe solar cells with different back contact configurations with and without MoO_2 (inset belongs to SEM top view of the absorber of each cell): a) Mo_3, b) Mo_3-$10MoO_2$ and c) Mo_3-$20MoO_2$ back contacts. (Note that CZTSe cells based on Mo_2 are similar to the ones based on Mo_3).
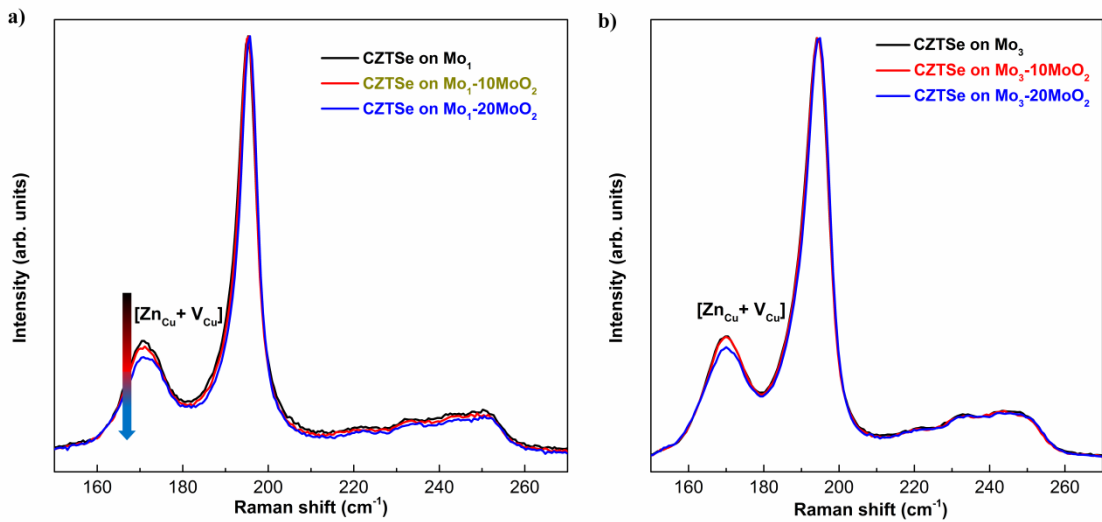
Figure 9. Raman spectra of CZTSe samples grown on different back contact configurations: a) Mo_1, Mo_1-$10MoO_2$ and Mo_1-$20MoO_2$ and b) Mo_3, Mo_3-$10MoO_2$ and Mo_3-$20MoO_2$. All Raman spectra are measured with 532 nm excitation

wavelength. The arrow indicates changes in the intensity of B modes correlating with the back contact modification.
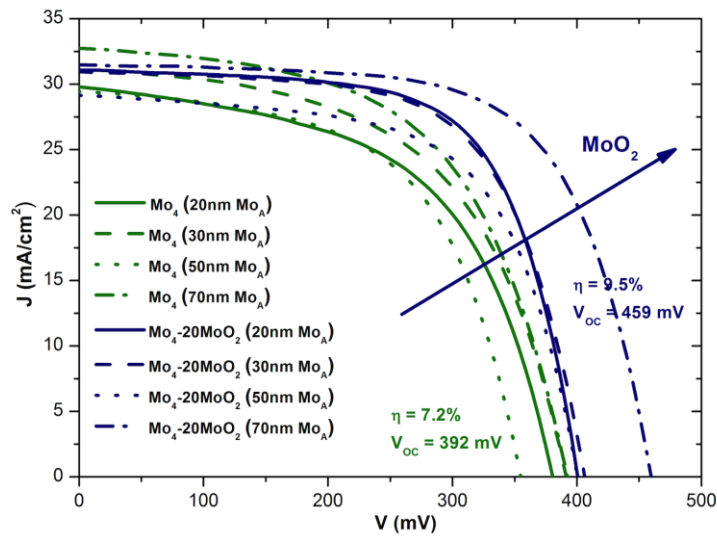
Figure 10. J-V illuminated curves of CZTSe cells based on Mo_4 tri-layers with different thickness of cap layer (20, 30, 50 and 70 nm) with and without a 20 nm underlying MoO_2 layer.
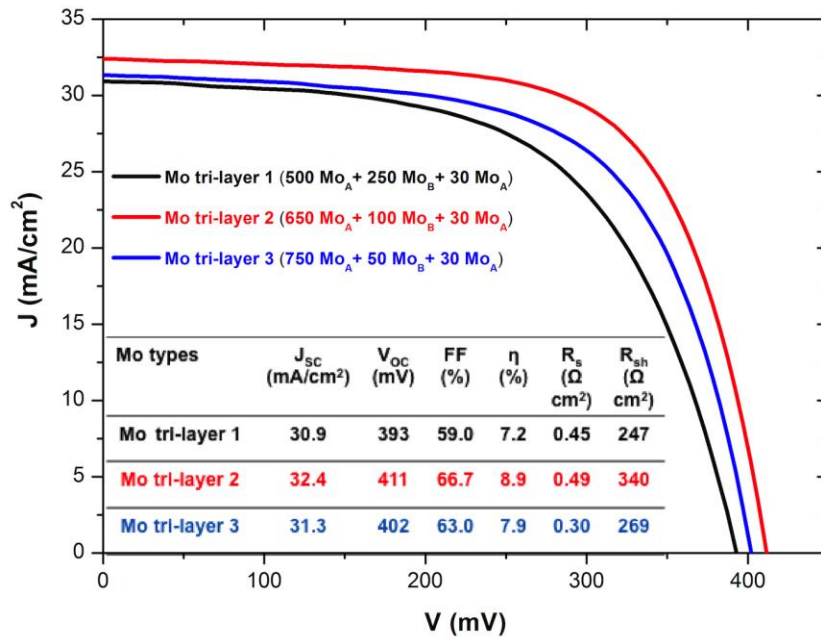
Figure 11. J-V illuminated curves of different Mo tri-layers (Mo_4 type) relying on different thickness of Mo_A and Mo_B constituent layers.

Graphical abstract
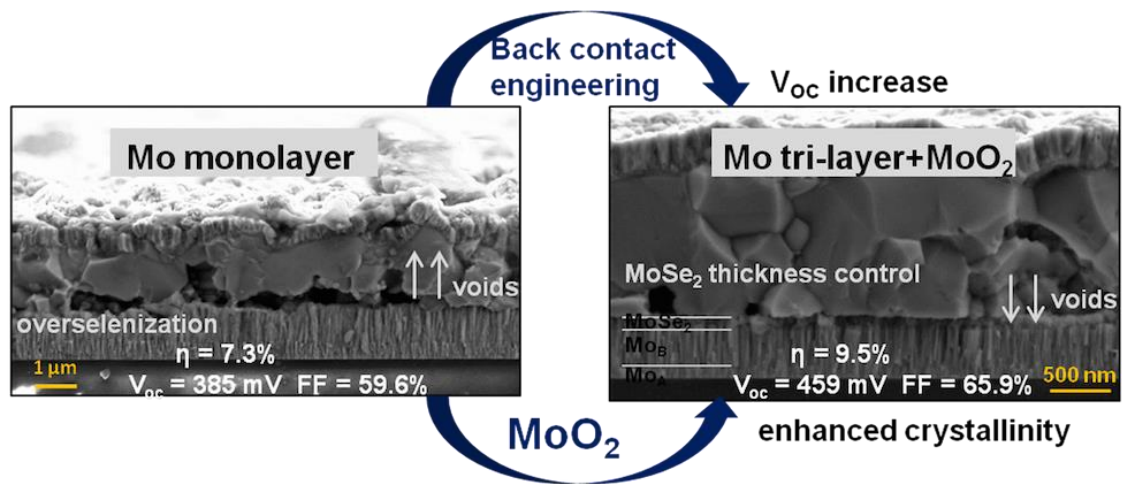
Research highlights

- Several Mo configurations (mono-, bi- and tri- layers) tested in CZTSe solar cells.

- Mo tri-layer avoids overselenization and effectively controls $MoSe_2$ thickness.

- Nanometric MoO_2 prevents overselenization, increases CZTSe grain size and solar cell efficiency.

- Efficiency improvement from 7.2% to 9.5% with large enhancement of V_{OC}, FF and R_{SH}.

- One of the highest V_{OC} for CZTSe technology 459 mV is obtained using 20 nm of MoO_2.

Supporting Information

The Importance of Back Contact Modification in Cu$_2$ZnSnSe$_4$ Solar Cells: the Role of a Thin MoO$_2$ Layer

Simon Lopez-Marino,[a,b]* Moisés Espíndola-Rodríguez[a], Yudania Sánchez[a], Xavier Alcobé[c], Haibing Xie[a], Florian Oliva[a], Markus Neuschitzer[a], Sergio Giraldo[a], Marcel Placidi[a], Raquel Caballero[d], Victor Izquierdo-Roca[a], Alejandro Pérez-Rodríguez[a,e], and E. Saucedo[a]

[a] Catalonian Institute for Energy Research (IREC), Jardin de les Dones de Negre 1, 08930, Sant Adrià del Besòs, Spain
[b] Present address: Crystalsol GmbH, Simmeringer Hauptstraβe 24, 1110, Vienna, Austria
[c] Centres Científics i Tecnològics de la Universitat de Barcelona (CCiTUB). LLuís Solé i Sabarís 1-3, 08028, Barcelona, Spain
[d] Universidad Autónoma de Madrid, Applied Physics Department
Francisco Tomás y Valiente 7, 28049 Madrid, Spain
[e] Departament de Electrònica (IN2UB), Universitat de Barcelona, Martí i Franquès 1, 08028, Barcelona, Spain

This supporting material includes additional morphological, structural, compositional and optoelectronic characterization to further support and highlight the relevance of back contact modification in CZTSe solar cells.

Experiment 1

The commonly reported degradation at the back contact for CZTSSe devices can be easily noticed in Figure S1. A large MoSe$_2$ layer of about 1 μm is observed along with a rough interface with many voids. This back interface degradation has been linked with a reduction in optoelectronic parameters of solar cells.[S1, S2]
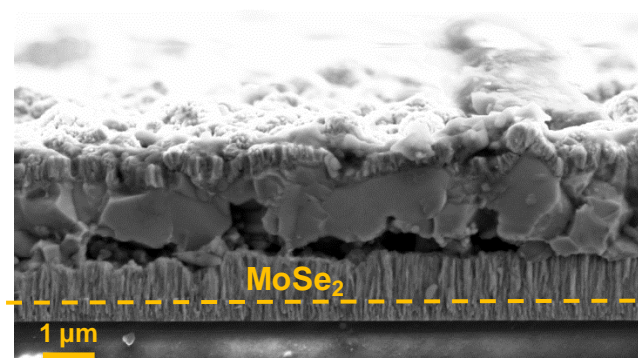
Figure S1. SEM cross sectional image of a full CZTSe solar cell based on a Mo monolayer, analogue to the Mo_1 type back contact.

To avoid the undesired effects of overselenization different Mo compound structures were tested based on different Mo deposition conditions. These conditions are summarized in the main document in Table 1. As a consequence of using different sputtering conditions the structural, morphological and electrical properties of the Mo will be affected.

Differences in morphology can be checked in Figure S2 via SEM images of Mo_A (a) and Mo_B (b). Additionally SEM cross sectional views of both Mo types are shown as insets.
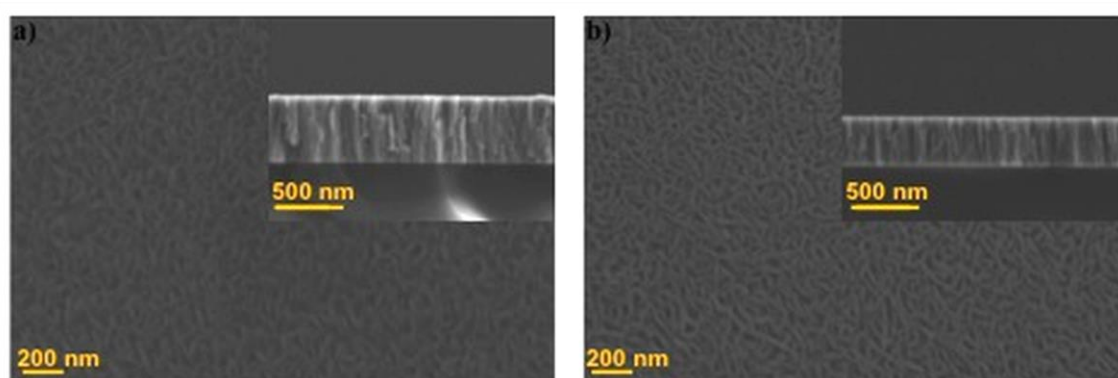
Figure S2. SEM top view image of Mo_A type (a) and Mo_B type (b). Additionally, SEM cross sectional views of both Mo layers are included as insets.

Figure S2 shows the typical columnar growth with elongated Mo grains for Mo layers obtained at lower pressure regimes, for both Mo_A (a) and Mo_B (b). Nevertheless, by focusing on the top view SEM images, Mo_A seems to have a more compact structure with less inter-granular space. In contrast, more voids between the grains can be seen in Mo_B. This is in agreement with the literature, since higher pressures are related to less dense Mo layers with more porosity.[S3-S5] Regarding the electrical features Mo_A (800 nm) has a sheet resistance of about 0.2-0.3 Ω/sq whereas Mo_B (500 nm) has a much higher sheet resistance of about 1.2 Ω/sq. These high values of sheet resistance are clearly reduced when using combined structures as the ones presented in the main document in Figure 1 (Experiment 1). The sheet resistance values of these Mo compound configurations are summarized in Table 2 of the same document.

In Figure S3 a comparison of the different behavior against selenization between different Mo back contacts, Mo_1, Mo_2 and Mo_3 is shown via XRD characterization. The contribution of different crystalline orientations of the $MoSe_2$ can be observed, due to the change in the c-axis orientation. The (002) diffraction plane belongs to the c-axis being perpendicular to the substrate, the 100 and the 110 diffraction peaks belong to the c-axis oriented parallel to the substrate and the 103 has been assigned to a mixture of both orientations.[S6, S7]
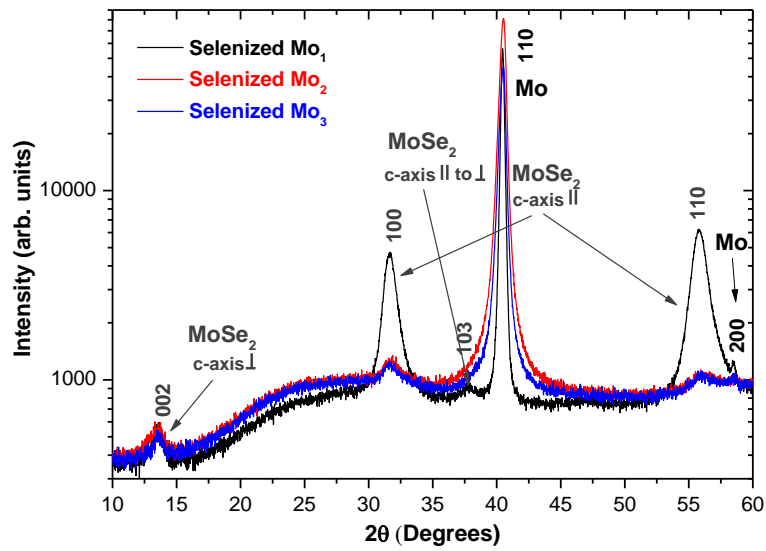
Figure S3. XRD patterns of selenized Mo_1, Mo_2 and Mo_3 back contact configurations. Different crystalline orientations of the $MoSe_2$ can be noticed due to a change in the c-axis orientation.

Raman spectroscopy is a surface sensitive powerful technique to assess structural and compositional features of analyzed samples. A green excitation laser source, 532.5 nm was used to characterize some of the investigated back contacts after the selenization process. Figure S4 shows the Raman spectra for the case of the selenization of a Mo_1 monolayer and its combination with 10 and 20 nm of MoO_2 combined with a 30 nm sacrificial cap Mo_A layer.
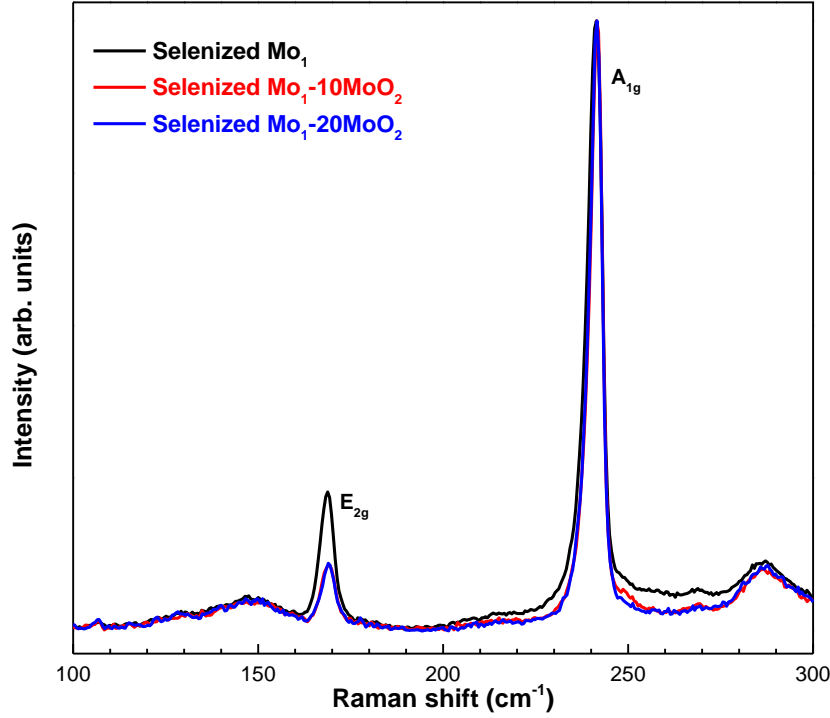
Figure S4. Raman spectra of different back contact configurations based on a monolayer Mo_1 structure after selenization, with and without a 10 and 20 nm MoO_2 layer combined with a 30 nm Mo_A cap layer.

At a first glance, the ratios between the most intense mode A_{1g} and the lower frequency and less intense E_{2g} mode are different when introducing the MoO_2 layer. Therefore, a change in texture occurs when introducing the MoO_2 layer, motivated by changes in the $MoSe_2$ orientation induced by the MoO_2 layer as it was previously confirmed by bulk oriented results obtained by XRD (See Figure 4a of the main document).[S8]

It is very important to take into account that the laser penetration depth in these analyses will be no more than 50 nm, and thereby in contrast with the results obtained by XRD they are surface sensitive.

Raman analyses were performed in Mo_3 bi-layer configurations with different thickness of MoO_2 layer to assess the change in texture of the $MoSe_2$ created after the

selenization of these back contact designs. The spectra obtained are shown next in Figure S5.
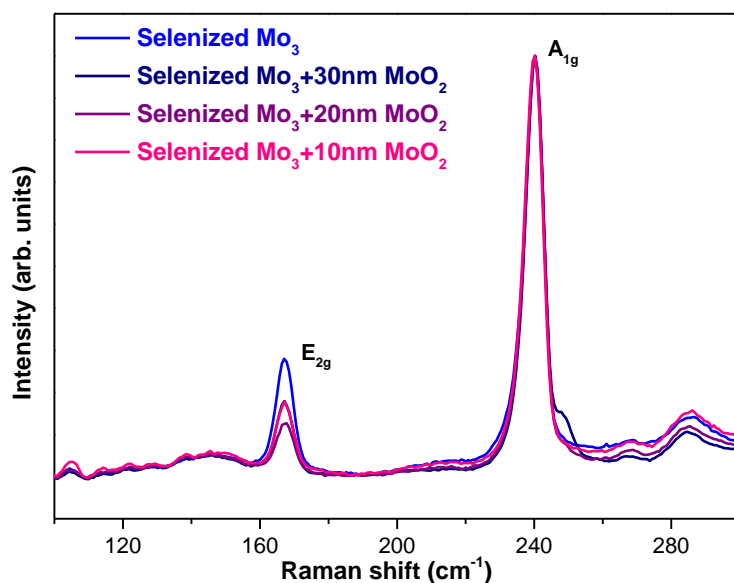
Figure S5. Raman spectra of different back contact configurations based on a bi-layer Mo_3 structure after selenization, with and without a 10, 20 and 30 nm MoO_2 layer (No additional Mo_A cap layer is included)

Again a clear change in texture for the $MoSe_2$ layers of the samples surface can be noticed when introducing the MoO_2 layer (change in the relative intensity of A_{1g} and E_{2g} modes). It has to be noted that since the MoO_2 layer cannot be selenized, the $MoSe_2$ detected when the MoO_2 is applied on top of the Mo_3 layer (with no Mo_A cap layer) might come from local areas with uncompleted MoO_2 coverage or cracks. Thus, generation of some $MoSe_2$ underneath the MoO_2 layer might take place.

It is very interesting to observe in Figure S6 the impact on the back contact interface morphology when using monolayers (Mo_1) and bi-layers (Mo_2). The overselenization effect coupled to Mo_1 creates a rough interface full of voids compared with the almost non selenized and smooth back interface from the cell based on Mo_2.
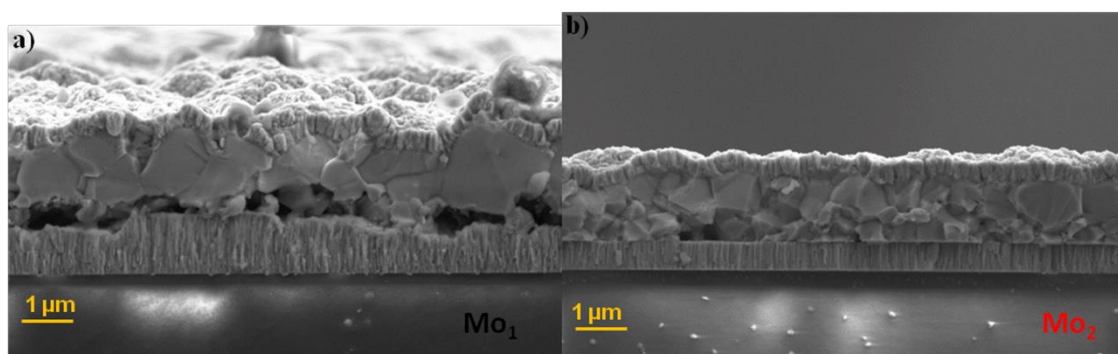
Figure S6. SEM cross sectional image of full CZTSe solar cells based on different back contact configurations; a) CZTSe cell based on Mo_1 back contact with back interface degradation with thick $MoSe_2$ layer and several and large voids; b) CZTSe cell based on Mo_2 back contact with even back interface morphology, very thin $MoSe_2$ and few voids.

In order to cope with overselenization it seems clear that a bi-layer configuration performs adequately, but the solar cells based on this layer suffer from degradation in optoelectronic parameters (see Figure 6 in the main document). We have correlated this problem with an almost negligible $MoSe_2$ layer between the CZTSe and the Mo. As a result a tri-layer configuration based on a bi-layer with a sacrificial and easily selenized Mo_A cap layer could allow for an effective $MoSe_2$ thickness tuning. Figure S7, shows a tri-layer configuration (Mo_4), based on a 30 nm Mo_A cap layer. As a result about 100 nm of $MoSe_2$ are formed.
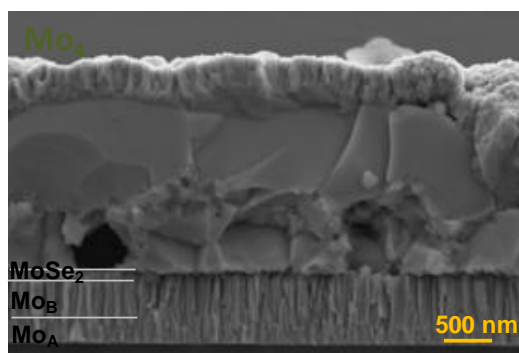

Figure S7. SEM cross sectional image of a full CZTSe solar cell based on a tri-layer configuration (Mo_4) with a 30 nm Mo_A cap layer as top part of the structure. Approximately 100 nm of $MoSe_2$ have been formed between CZTSe and Mo_A+Mo_B

All the back contacts investigated in experiment 1 were tried as part of full CZTSe solar cells. Figure S8 shows the statistical spread of the main optoelectronic parameters for 12 cells processed with Mo_1 and Mo_3 with their combinations with 10 or 20 nm of MoO_2 layer with a 30 nm Mo_A cap layer (results for the cells based on Mo_2 are relatively similar to the ones obtained for Mo_3, reaching the same value for the maximum efficiency obtained with Mo_3 and 20 nm of MoO_2). It can be easily noticed that almost all the optoelectronic parameters improved when introducing the MoO_2 layer, especially for the case of 20 nm MoO_2 layer. In the case of Mo_1 when using 10 nm MoO_2 layer we believe some processing damage could have affected the final results, since there is a clear trend when comparing the non MoO_2 based case for Mo_3 with its oxide containing counterparts (almost a linear trend can be drawn with the mean optoelectronic parameters values, see Figure S8 e, f, g, h). Similar results were obtained for Mo_2 but they are not shown for simplicity reasons. It is also interesting to see how the J_{SC} values based on Mo_1 are systematically larger than the ones based on Mo_3; 31.9 mA/cm^2 against 28.6 mA/cm^2 for the mean J_{SC} value for Mo_1 and Mo_3 respectively. As it was already mentioned in the main document this correlates with the type of deposition conditions used to produce Mo_1, leading to a highly conductive and compact Mo structure.
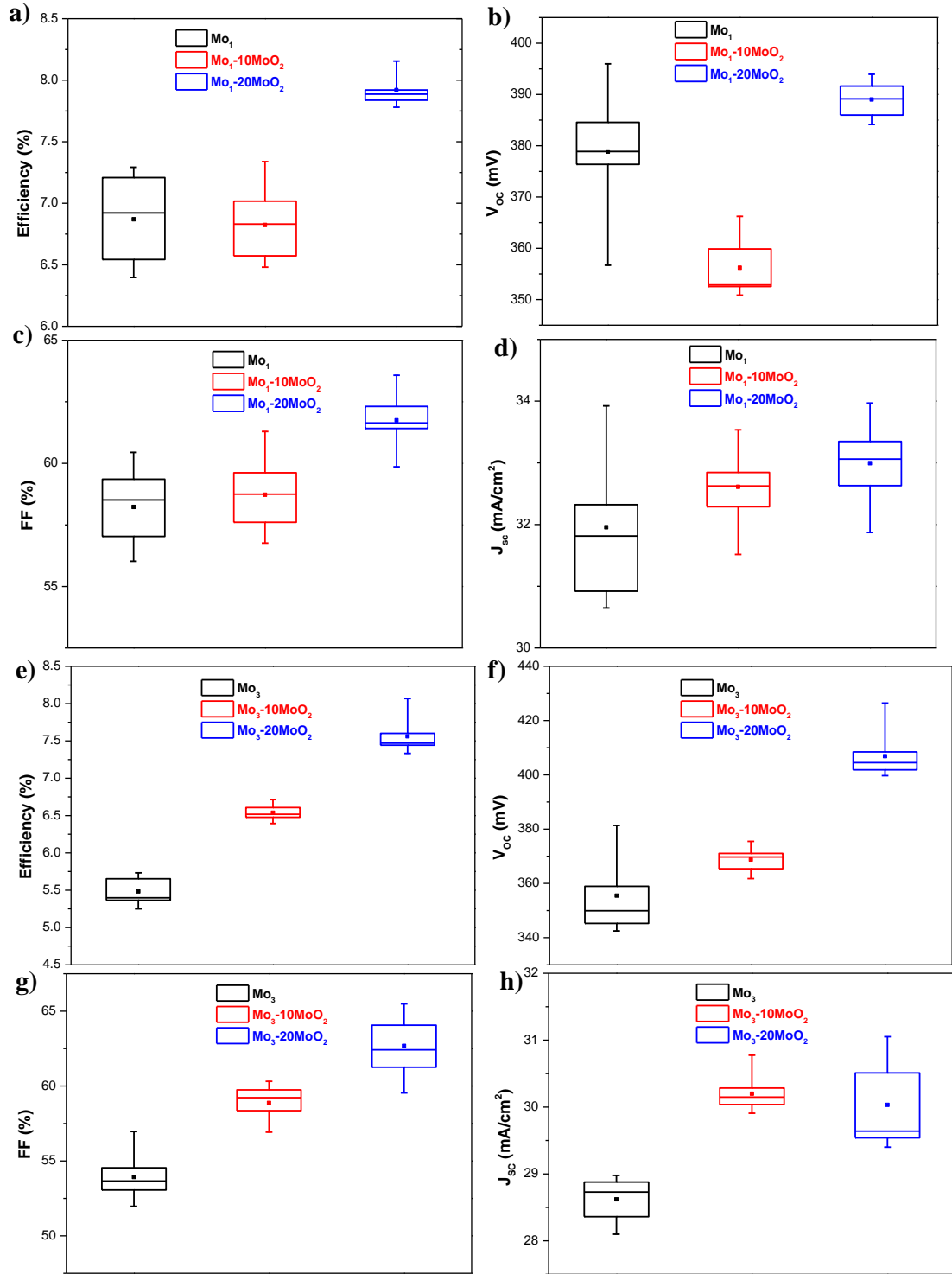
Figure S8. Statistical spread of main optoelectronic parameters from 12 cells processed in experiment 1 with Mo_1 and Mo_3 series and their combination with 10 and 20 nm intermediate MoO_2 layer: Efficiency (a,e), V_{OC} (b,f), FF (c,g) and J_{SC} (d,h). Note that the solid square represents the mean value.

As a result of the introduction of the MoO_2 intermediate layer an important increase in grain size has been observed in the SEM cross section of completed CZTSe devices (See Figure 8 of main document). Additional top SEM images of CZTSe absorbers from full solar cells (buffer layer and TCO were previously etched in diluted HCl) based on the back contact designs from Experiment 1 are shown in Figure S9.
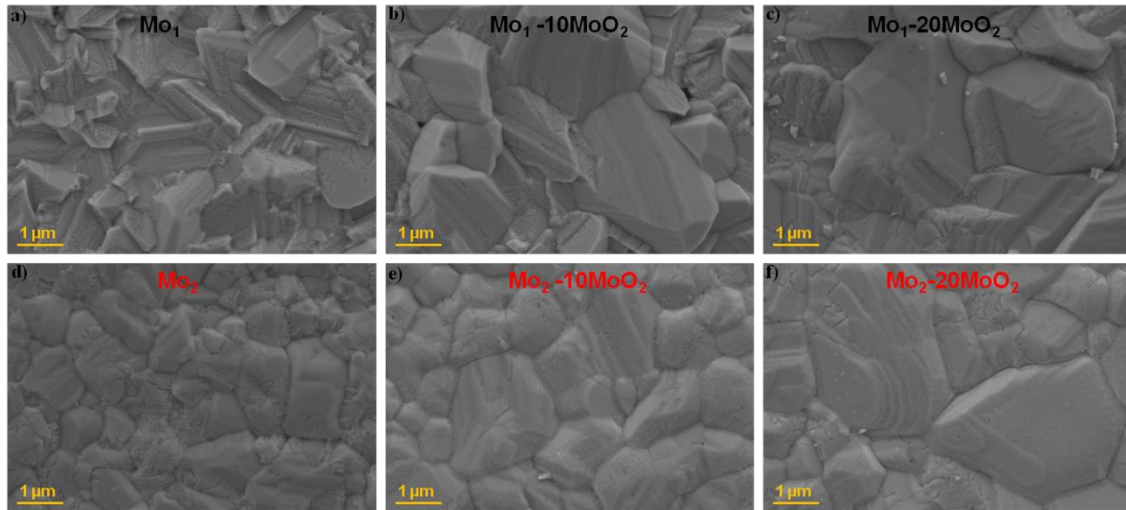
Figure S9. Top view of CZTSe absorbers from full solar cells based on Mo_1 (a), Mo_1-10MoO_2 (b), Mo_1-20MoO_2 (c), Mo_2 (d), Mo_2-10MoO_2 (e) and Mo_2-20MoO_2 (f).

It is clear that the introduction of the intermediate MoO_2 layer systematically enhances the grain growth of CZTSe absorbers regardless the type of Mo back contact used. Nevertheless, it is interesting to compare the differences in morphology of CZTSe grains when different types of Mo configurations are used. Whereas Mo monolayers (Figure S9a) induce sharper grains with more 2D defects such as twin boundaries, the use of Mo bi-layer structures (Figure S9d) tends to produce rounded grains with a much softer topography. The reason is clearly due to relevant structural differences between the analyzed Mo types, giving rise to different microstrains in the Mo layer and different inter-granular space, and thereby different features in terms of impurities (such as alkaline elements) diffusion and adsorption.

Since the sintering of the absorber is usually linked with the Na content, TOF-SIMS elemental depth profiles of a cell without MoO_2 and with the oxide are shown next in Figure S10 in order to confirm whether the Na diffusion has been modified or not.
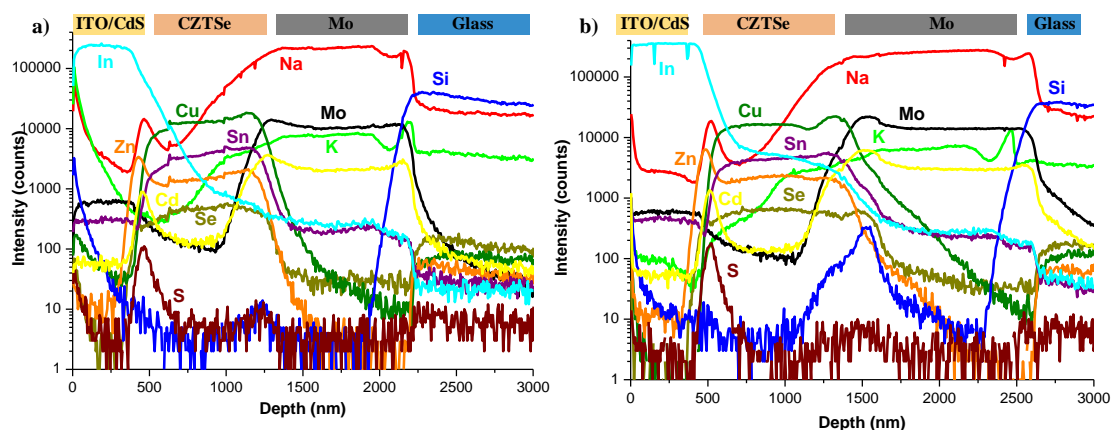
Figure S10. TOF-SIMS elemental depth profile of completed CZTSe solar cells based on different back contact configurations: a) CZTSe cell on Mo_2; b) CZTSe cell on Mo_2-20nmMoO_2.

The alkali content is relatively similar in the absorber and no significant variations can be drawn after the introduction of the 20 nm MoO_2 layer. Likewise, the Na elemental depth profile for the 10 nm MoO_2 sample (not shown) has very similar distribution across the solar cell.

Raman spectroscopy was performed on CZTSe absorbers grown on different back contact configurations (Mo_1, Mo_1-10MoO_2, Mo_1-20MoO_2, Mo_1-30MoO_2, Mo_3, Mo_3-10MoO_2, Mo_3-20MoO_2 and Mo_3-30MoO_2). A summary with FWHM, Raman shift of the dominant A mode, and ratio between the intensity of the peak at the 170 cm^{-1} spectral region and the peak of the most intense A mode (I_{170}/I_{195}) is shown in Table S1:

	Mo$_1$	Mo$_1$-10MoO$_2$	Mo$_1$-20MoO$_2$	Mo$_3$	Mo$_3$-10MoO$_2$	Mo$_3$-20MoO$_2$
Raman shift (cm^{-1})	195.18	195.29	195.58	194.32	194.35	194.60
FWHM (cm^{-1})	5.80	5.55	5.33	8.50	8.40	8.20
I$_{170}$/I$_{195}$	0.694	0.538	0.529	0.401	0.373	0.284

Table S1. Summary of parameters obtained from Raman spectra of different CZTSe absorbers grown on Mo$_1$, Mo$_1$-10MoO$_2$, Mo$_1$-20MoO$_2$, Mo$_3$, Mo$_3$-10MoO$_2$, and Mo$_3$-20MoO$_2$ back contact designs. The parameters are FWHM, Raman shift of the main peak and ratio between the intensity of the peak at the 170 cm^{-1} spectral region and the peak of the most intense A mode (I$_{170}$/I$_{195}$).

It can be concluded that the addition of the MoO$_2$ layer enhances the crystalline quality of CZTSe absorbers regardless the type of Mo used. This is confirmed by the reduction of the FWHM and the increase of the Raman shift of the main dominant peak. Moreover, the CZTSe crystalline quality from a monolayer configuration (Mo$_1$) seems to be higher than the CZTSe grown on a bi-layer configuration (Mo$_3$). Another relevant feature is the reduction of the relative intensity of the Raman mode around 170 cm^{-1} spectral region when the MoO$_2$ is applied. This is related with a Cu depleted surface and the promotion of [Zn$_{Cu}$ + V$_{Cu}$] defect clusters.[S9]

A summary of the main compositional ratios is shown in Table S2 next:

	Mo$_1$	Mo$_1$-10MoO$_2$	Mo$_1$-20MoO$_2$	Mo$_3$	Mo$_3$-10MoO$_2$	Mo$_3$-20MoO$_2$
Cu/(Zn+Sn)	0.75	0.75	0.74	0.77	0.77	0.77
Zn/Sn	1.13	1.14	1.05	1.17	1.20	1.17
Cu/Sn	1.60	1.61	1.51	1.68	1.69	1.82

Table S2. Summary of Cu/(Zn+Sn), Zn/Sn and Cu/Sn compositional ratios for CZTSe absorbers grown on Mo$_1$, Mo$_1$-10MoO$_2$, Mo$_1$-20MoO$_2$, Mo$_3$, Mo$_3$-10MoO$_2$ and Mo$_3$-20MoO$_2$ back contact designs.

It can be concluded that non relevant compositional changes for Cu/(Zn+Sn) (0.74-0.77) are noticeable. Slightly larger variations were obtained for the Zn/Sn ratio, 1.05-

1.20 and for the Cu/Sn, 1.51-1.82, but every type of back contact should be compared separately in order to assess changes in the Raman spectra of Figure 8 from the main document. According to the literature, these compositional variations could not account for the Raman peaks changes observed.[S9]

Clear evidences of the benefits of the MoO_2 layer were presented but could this oxide be used on top of the investigated Mo configurations without any Mo_A cap layer on top? CZTSe solar cells based on Mo_1 and Mo_3 back contacts prepared with MoO_2 evaporated on top of them with no Mo_A sacrificial cap layer were produced to answer the question. MoO_2 layers of 10, 20 and 30 nm were investigated. It has to be noted that these particular cases with no Mo_A cap layer were characterized by XRD in Figure 5. The main optoelectronic parameters of these cells are shown next in Table S3:

Mo types	J_{SC} (mA/cm^2)	V_{OC} (mV)	FF (%)	η (%)	R_s (Ω cm^2)	R_{sh} (Ω cm^2)
Mo_1	31.9	394	61.1	7.7	0.8	165
Mo_1+10MoO_2	26.3	267	50.9	3.6	0.8	73
Mo_1+20MoO_2	26.2	293	53.7	4.1	0.8	112
Mo_1+30MoO_2	23.4	262	52.0	3.2	0.9	82
Mo_3	29.9	361	58.2	6.3	0.8	115
Mo_3+10MoO_2	27.9	287	53.2	4.3	0.8	102
Mo_3+20MoO_2	24.4	204	43.6	2.2	1.3	29
Mo_3+30MoO_2	23.6	215	45.0	2.3	1.3	37

Table S3. Summary of optoelectronic parameters from CZTSe solar cells based on Mo_1, Mo_1-10MoO_2, Mo_1-20MoO_2, Mo_1-30MoO_2, Mo_3, Mo_3-10MoO_2, Mo_3-20MoO_2, and Mo_3-30MoO_2 with no Mo_A cap layer grown on top of any of these back contact designs.

When no Mo_A sacrificial cap layer is part of the Mo back contact designs a degradation of the solar cells performance seems to correlate with the MoO_2 layer

thickness, reaching the poorest performance for the 30 nm case. A remarkable decrease in V_{OC} of about 130-150 mV and FF around 10-15 % absolute value can be noticed. Likewise the photocurrent (J_{SC}) decreases 7-9 mA/cm^2 in absolute value, correlating with an increase in the series resistance (Rs), specially for the Mo_3 bi-layer case.
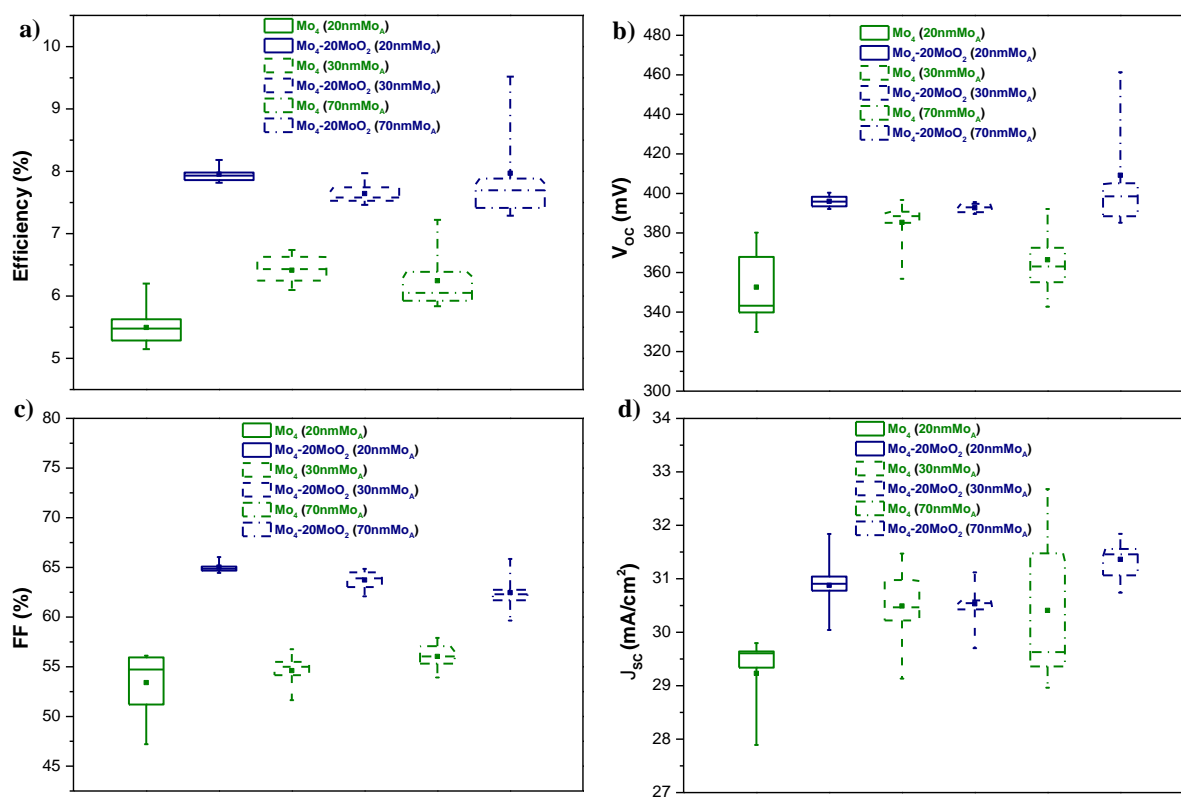
Experiment 2

Experiment 2 of the main document dealt with the influence of the thickness of a cap layer being part of a tri-layer Mo configuration on the performance of CZTSe solar cells. After selenization, this cap layer would give rise to different layers in thickness of $MoSe_2$, since it is easily selenized as proved in Figure 3 of the main document and Figure S1 of this supporting information. Table S4 shows the evolution of $MoSe_2$ thickness with increasing Mo_A cap layer thickness. A fine tuning from about 80 to 120 nm was achieved when going from 20 to 70 nm of Mo_A top layer.

Sample name	$MoSe_2$ (nm)	Remaining Mo (nm)
Mo_4 (20nm Mo_A)	84	705
Mo_4 (30nm Mo_A)	81	709
Mo_4 (50nm Mo_A)	97	729
Mo_4 (70nm Mo_A)	117	723

Table S4. XRF estimated values for the thickness of both $MoSe_2$ formed after selenization of Mo_4 tri-layers with different Mo_A cap thickness, and non selenized Mo after the same annealing process.

The statistical spread of the main optoelectronic parameters extracted from the illuminated J-V curves of 12 cells processed using tri-layers (Mo_4) configurations based on 20, 30 and 70 nm of Mo_A cap layers and their 20 nm MoO_2 based counterparts are shown in Figure S13. As it was mentioned in the main document due

to a suspected lower performance associated to process failures, samples relying on
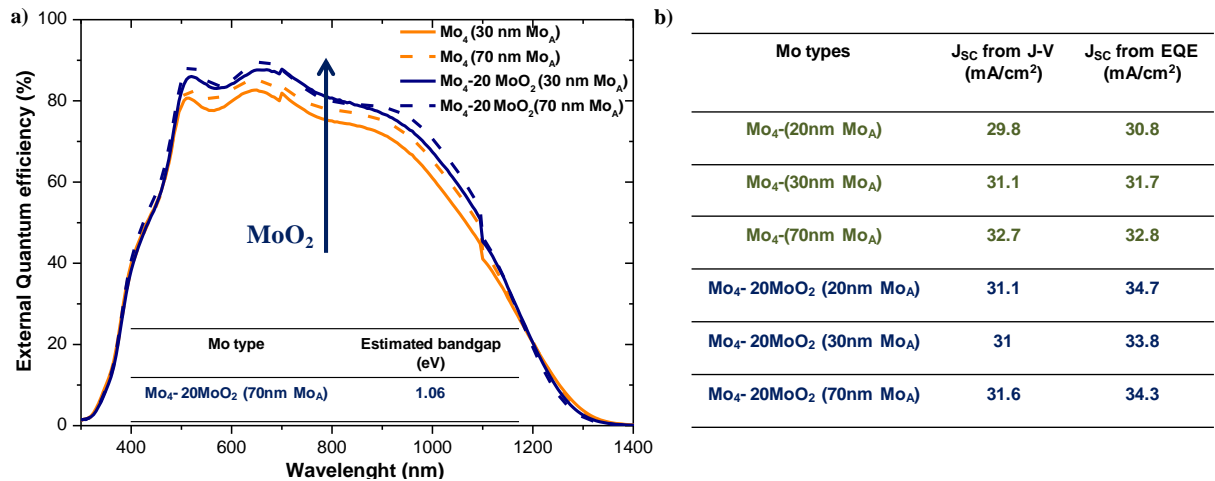
the 50 nm Mo_A case are not included.

Figure S11. Statistical spread of main optoelectronic parameters from 12 cells processed in experiment 2 with Mo_4 with 20,30 and 70 nm of Mo_A and their combinations with 20 nm intermediate MoO_2 layer: Efficiency (a), V_{OC} (b), FF (c) and J_{SC} (d). Note that the solid square represents the mean value.

In general all the parameters increase after the introduction of MoO_2 as part of the

back contact structure (only J_{SC} in the case of maximum values is slightly lower than

the reference case for 30 nm and 70 nm Mo_A cap layer)

In experiment 1 a major improvement in photocurrent collection when the MoO_2 was

applied was observed for all the absorption range, although the change in Jsc from J-

V curves was not significant. In experiment 2 a similar change was noticeable

although this time most of the J_{SC} values for the MoO_2 containing samples were even

slightly lower than the ones obtained via J-V curves. Figure S12a shows the EQE

plots for the Mo_4 cases with 30 and 70 nm cap layer and their related MoO_2 counterparts. It should be noted that other cases are not shown for reasons of simplicity. As it was previously observed in the main document, an important increase across the whole absorption spectrum is observed for the EQE of samples containing the MoO_2. This could be explained by light induced defects caused by white and strong light coming from the solar simulator. These light active defects could increase recombination processes reducing the minority charge collection. Additionally, reflection effects related to changes in the morphology of CZTSe absorbers could also contribute to this change in the J_{SC} value. Figure S12b summarizes in a table the values of the photocurrent extracted from J-V plots and from EQE. When focusing on the cases of Mo_4 variations without MoO_2 layer the differences are not larger than 1 mA/cm^2 which is the error of the measurement. In the case of the MoO_2 Mo_4 back contact variations, in all the cases the difference is close to 3 mA/cm^2 or even larger.

Mo types	J_{SC} from J-V (mA/cm^2)	J_{SC} from EQE (mA/cm^2)
Mo_4-(20nm Mo_A)	29.8	30.8
Mo_4-(30nm Mo_A)	31.1	31.7
Mo_4-(70nm Mo_A)	32.7	32.8
Mo_4- 20MoO_2 (20nm Mo_A)	31.1	34.7
Mo_4- 20MoO_2 (30nm Mo_A)	31	33.8
Mo_4- 20MoO_2 (70nm Mo_A)	31.6	34.3

Figure S12. EQE plots of Mo_4 tri-layer configurations with different cap layer thicknesses and with and without a 20 nm underlaying MoO_2 layer (a); table/summary of the comparison of J_{SC} values for some Mo_4 cases of Experiment 2 extracted from J-V curves and EQE (b).

Additional references

[S1]   S. Lopez-Marino, M. Placidi, A. Perez-Tomas, J. Llobet, V. Izquierdo-Roca, X. Fontane, A. Fairbrother, M. Espindola-Rodriguez, D. Sylla, A. Perez-Rodriguez, E. Saucedo, J. Mater. Chem. A. 1 (2013) 8338-8343.

[S2]   B. Shin, Y. Zhu, N. A. Bojarczuk, S. J. Chey, S. Guha, Appl. Phys. Lett. 101 (2012) 053903.

[S3]   C. Roger, S. Noël, O. Sicardy, P. Faucherand, L. Grenet, N. Karst, H. Fournier, F. Roux, F. Ducroquet, A. Brioude, S. Perraud, Thin Solid Films. 548 (2013) 608-616.

[S4]   P.M.P. Salomé, J. Malaquias, P.A. Fernandes, A.F.d. Cunha, J. Phys. D: Appl. Phys. 43 (2010) 345501.

[S5]   J.H. Scofield, A. Duda, D. Albin, B.L. Ballard, P.K. Predecki, Thin Solid Films. 260 (1995) 26-31.

[S6]   D. Abou-Ras, D. Mukherji, G. Kostorz, D. Brémaud, M. Kälin, D. Rudmann, M. Döbeli, A. N. Tiwari, MRS Online Proc. Lib. 865 (2005) F8.1.

[S7]   R. Würz, D. Fuertes Marrón, A. Meeder, A. Rumberg, S.M. Babu, T. Schedel-Niedrig, U. Bloeck, P. Schubert-Bischoff, M.C. Lux-Steiner, Thin Solid Films. 431-432 (2003) 398-402.

[S8]   T.J. Wieting, J.L. Verble, Phys. Rev. B. 3 (1971) 4286-4292.

[S9]   M. Dimitrievska, A. Fairbrother, E. Saucedo, A. Pérez-Rodríguez, V. Izquierdo-Roca, Appl. Phys. Lett. 106 (2015) 073903.